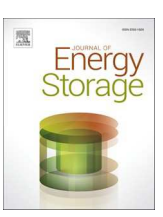
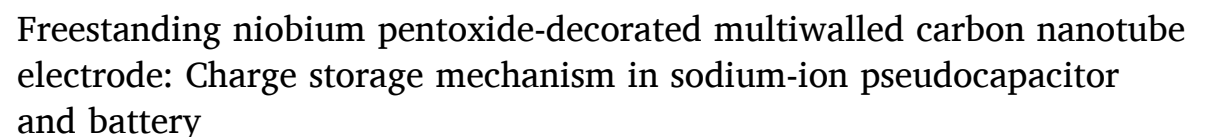
Contents lists available at ScienceDirect

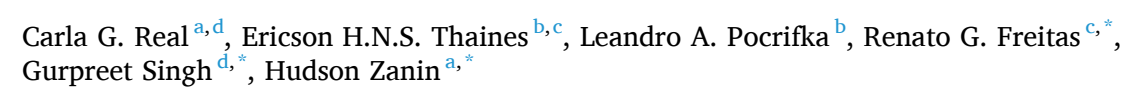
Journal of Energy Storage

journal homepage: www.elsevier.com/locate/est



Research papers





- a Advanced Energy Storage Division, Carbon Sci-Tech Labs, Center for Innovation on New Energies, School of Electrical and Computer Engineering, University of Campinas, Av Albert Einstein 400, Campinas, SP, Brazil
- Department of Chemistry, Laboratory of Electrochemistry and Energy, Federal University of Amazonas, Manaus, AM, Brazil
- Institute of Physics & Department of Chemistry, Laboratory of Computational Materials, Federal University of Mato Grosso, Cuiabá, MT, Brazil

ARTICLE INFO

Keywords: Intercalation pseudocapacitance Sodium-ion devices Freestanding carbon nanotube electrode Niobium pentoxide

ABSTRACT

This study investigated flexible, freestanding niobium pentoxide (Nb₂O₅) decorated multiwalled carbon nanotube (MWCNT) electrode material in a sodium-ion pseudocapacitor and its respective energy storage mechanism. Sodium is an abundant element in the Earth's crust, with attractive sustainability and low-cost appeal for the scientific community and energy markets such as electric vehicles and renewable energies. Combined with niobium pentoxide and carbon nanotubes, sodium ions can perform ultra-fast intercalation into niobium pentoxide and electrostatic adsorption onto carbon high surface areas. Niobium pentoxide particles were investigated using X-ray diffraction via Rietveld refinement, a powerful technique to study crystalline materials' electronic and structural properties that directly influence Na+-ion diffusion. The niobium pentoxide-decorated MWCNT electrode material was investigated within a symmetric supercapacitor (SIC) and as an anode for sodium-ion batteries (SIBs). A finite-length transmission line was used to model the impedance behavior of the solid and liquid phases that comprised the material/solution interface. This numerical modelling allowed investigators to infer the presence of MWCNT as a nanostructured matrix since Nb₂O₅ dispersive nanoparticles increased the overall pseudopacacitance by 63.2% for Nb₂O₅/MWCNT compared to MWCNT nanostructured electrodes. Electrochemical findings revealed a maximum capacitance of 192 F g⁻¹ for the SIC full cell, with capacitance retention of 96% after 10,000 cycles. In addition, the SIC delivered outstanding power density from 98.7 to 24,671 W kg⁻¹ and high energy density from 5.4 to 2.7 W h kg⁻¹. In an SIB half-cell configuration, the electrode delivered a reversible sodium-ion storage capacity of \sim 163 mA h g $^{-1}$, with a retention capacity of \sim 68 mA h g $^{-1}$ after 100 cycles at 25 mA $\rm g^{-1}$. These systems bridge the gap between supercapacitors and batteries by employing the best properties of them both.

1. Introduction

Energy storage devices (ESDs) are under constant development due to increasing demands for high energy and power densities for expanding renewable and energy storage infrastructures. Portable electronics, wearables, electric vehicles, and renewable energy sources comprise a multibillion-dollar ESD market, and the need for extended storage energy and more rapid charge time means the ideal ESD should utilize supercapacitors and metal-ion batteries. Supercapacitors and

Received 30 December 2021; Received in revised form 29 April 2022; Accepted 2 May 2022

batteries are complementary devices when energy and power, respectively, are under consideration [1]. A supercapacitor is a power system, and a battery is a long-term energy storage device [2]. The energy storage process in supercapacitors primarily occurs via charge separation in a Helmholtz double layer at the electrode-electrolyte interface [3]. The main goal of ongoing supercapacitor research is to improve energy storage while maintaining the power system's long lifespan and power features [4], meaning capacitance and cell voltage must be enhanced. Combining carbon materials with transition metal oxides [5]

E-mail addresses: renato.sobrinho@ufmt.br (R.G. Freitas), gurpreet@ksu.edu (G. Singh), hzanin@unicamp.br (H. Zanin).

https://doi.org/10.1016/j.est.2022.104793

Available online 18 May 2022 2352-152X/© 2022 Published by Elsevier Ltd.

^d Alan Levin Department of Mechanical and Nuclear Engineering, Kansas State University, Manhattan, KS 00506, USA

^{*} Corresponding authors.

or conductive polymers [6] to introduce fast redox reactions [7] is one method to improve pseudocapacitance values.

Conversely, chemical energy in metal-ion batteries is converted into direct current electricity through redox reactions and intercalation processes. Although these processes are more energetic in the metal-ion batteries than in the supercapacitor, power density and cycle-life are the main drawbacks of metal-ion batteries [8]. Therefore, current research seeks to combine the power density of supercapacitors and the high energy density of batteries [9]. Reliable practice includes selecting materials that combine the time constant of fast faradaic reaction (diffusion-less processes) and the electrostatic adsorption/desorption (non-faradaic) process [10].

Among ESD technologies, Na⁺ ion-based devices have been intensively investigated as a promising alternative to Li⁺ ion-based devices for large-scale energy storage due to their similar electrochemical properties and the low cost of abundant sodium [11]. However, many challenges remain before Na⁺ ion-based devices become commercially competitive [12]. For example, compared to Li⁺-ion, the larger Na⁺-ion results in slower electrochemical kinetics and significant restrictions throughout the intercalation process, which may cause electrode damage, reduce performance, and decrease device lifespan [13]. Despite these drawbacks, extensive efforts have focused on the rational design of nanostructured and novel electrodes to improve Na⁺-ion transport kinetics suitable for rapid, reversible insertion and extraction of these ions [14].

One promising anode material for alkali metal-ion-based ESD is $\mathrm{Nb_2O_5}$ because it has high power characteristics and cycling stability due to its pseudocapacitive charge storage property [15–17]. Brauer et al. [18] described three $\mathrm{Nb_2O_5}$ -polymorphs: T- $\mathrm{Nb_2O_5}$ (orthorhombic crystal phase), M- $\mathrm{Nb_2O_5}$ (β -monoclinic crystal phase), and H- $\mathrm{Nb_2O_5}$ (α -monoclinic crystal phase). Frevel and Rinn [19] announced a new pseudohexagonal phase, TT- $\mathrm{Nb_2O_5}$ (pseudohexagonal crystal phase). The T-nomination comes from the German word *tief*, which means low, related to the low temperature; the B- polymorph refers to the crystal habit (*blätter* or bladed); and H- stands for "high," referring to the high-temperature phase. Because of it allows $\mathrm{Na^+}$ -ion intercalation/deintercalation processes, the T- $\mathrm{Nb_2O_5}$ crystalline phase has captured growing interest as a promising, fast-charging anode material [20–22], as suggested in the reaction below:

$$Nb_2O_5 + xNa^+ + xe^- = Na_xNb_2O_5 \tag{1}$$

Both T-Nb₂O₅ and H-Nb₂O₅ crystalline phases have promising, larger interplanar lattice spacing ($d_{(001)}=3.930$ Å for T-Nb₂O₅ and $d_{(101)}=3.802$ Å for H-Nb₂O₅) compared to the Na⁺-ion diameter (i.e., 1.060 Å), leading to more prompt sodiation/de-sodiation behaviors [23]. Consequently, the Nb₂O₅ crystalline phase exhibits specific planes that directly influence Na⁺-ion diffusion and warrant careful study. X-ray diffraction (XRD) via Rietveld refinement is an efficient technique to study crystalline materials' electronic and structural properties [24].

However, the poor electrical conductivity of the Nb₂O₅ material ($\sigma \sim 3 \times 10^{-6} \text{ S cm}^{-1}$) limits its practical application in ESDs, thereby requiring a keen electrochemical study to determine the figure of merits for ESDs. Furthermore, multiwalled carbon nanotubes (MWCNTs) and channels in T-Nb₂O₅ and H-Nb₂O₅ crystalline phases lead to defective electrode materials with irregular surface morphologies and structural disorders.

Porous/disordered electrode materials often result in "distributed capacitance" due the ions do not access all the electrode regions concomitantly during polarization [25,26]. Therefore, a single-valued capacitance is rarely achieved in disordered/porous electrodes [25]. However, electrochemical impedance spectroscopy (EIS) can be effective to obtain the distributed capacitance as a function of applied frequency even with dissipative effects. Electrochemical impedance studies have been implemented into transmission line (TL) models [27–31]. This research utilized the TL model to study nanostructured systems such as TiO₂-nanotubes [32], conductive polymers [33], carbon

nanofibers [25], NiO@MWCNT [34], MnO@MWCNT [35], and NiAl alloys as current collectors [36]. This study is thought to be the first to use the TL model to investigate Na⁺-ion ESDs.

The storage energy properties of $\mathrm{Nb_2O_5}$ materials may improve by combining heteroatoms, constructing nanostructures, or introducing a carbon matrix (e.g., carbon nanotubes or graphene) [16,28]. Tables S1 and S2 from Supplementary information gather some properties for carbon-based electrodes using sodium ion for ESD. Besides that, $\mathrm{Nb_2O_5}$ also shows promise for lithium-ion devices. For example, a publication of our group proposed by Vicentini et al. [16] studied $\mathrm{Nb_2O_5@MWCNT}$ nanostructures as the electrode for aqueous electrochemical capacitors. The authors observed that $\mathrm{Nb_2O_5@MWCNT}$ nanostructures had notable electrochemical properties, presenting high specific capacitance (\sim 320 F g $^{-1}$), long lifespan (more than 100,000 cycles), and high energy and power densities.

From the above considerations, the current study investigated the synthesis of a self-supported and binder-free electrode of $\mathrm{Nb}_2\mathrm{O}_5$ material decorated into MWCNTs. This material was used as electrodes in a symmetric Na^+ -ion supercapacitor and as a potential anode for a Na^+ -ion battery. We also presented an innovative TL model to investigate the device energy storage mechanism. Results indicated that the different properties between supercapacitors and batteries can be bridged by combining these materials.

2. Experimental

2.1. Materials

Optical grade niobium pentoxide (Nb $_2$ O $_5$ 99.8% purity) was received via Brazilian Metallurgy and Mining Company (CBMM) donation. Carbon nanotubes Ctube-120 MWCNTs (95% purity diameter of 10–40 nm, length of 1.0–40 µm) were obtained from the CNT Korea Co., Ltd. Carbon black and Black Pearls® 2000 were purchased from Cabot, and polyvinylidene fluoride (PVDF), sodium perchlorate (NaClO $_4$), ethyl carbonate (EC), and dimethyl carbonate (DMC) were purchased from Sigma-Aldrich.

In this work, three different electrode types were used to evaluate the behavior of the Nb_2O_5 composites: a paint on copper foil and two buckypapers [one constituted of MWCNT and the other, with Nb_2O_5 added]. The electrodes were fabricated as described in the following section.

2.2. Preparation of Nb₂O₅ paint electrode

The carbon black and the Nb₂O₅ (1:4 wt/wt) were ground in a ball mill for 1 h to ensure the mix between them. The mixture was placed in a crucible in a Chemical Vapor Deposition (CVD) oven at 800 °C for 1 h with an increased rate of 5 °C minute⁻¹ in an N₂ atmosphere. Cooling down the oven, the mixture was added to a solution of PVDF and N-Methylpyrrolidone (NMP) in a proportion of 70% Nb₂O₅, 15% carbon black, and 15% PVDF. The solution was sonicated for 30 min and deposited onto a copper foil using a doctor blade coating, as presented in Fig. 1a. The system was then dried for 1 h at 60 °C and 1 h at 80 °C and then placed overnight into a vacuum oven for solvent removal. After dried, circular cells were cut (d=1.6 cm, $m_{total}=18$ mg, $m_{copper}=17$ mg, $m_{active}=0.9$ mg, $\varepsilon_{total}\approx17$ µm $\varepsilon_{copper}\approx15$ µm) to be the working electrode in a coin cell (model CR2032) scheme.

2.3. Preparation of MWCNT and $Nb_2O_5/MWCNT$ self-supporting electrodes

Two buckypapers were developed, referred to hereafter as MWCNT and $\rm Nb_2O_5/MWCNT$ materials. For this, two precursor solution consisting of 30 mg of MWCNT, 200 mg of sodium dodecyl sulfate (SDS), and 200 mL of deionized water (DI) were prepared. SDS was added to increase the interaction between MWCNT and water which, due to its

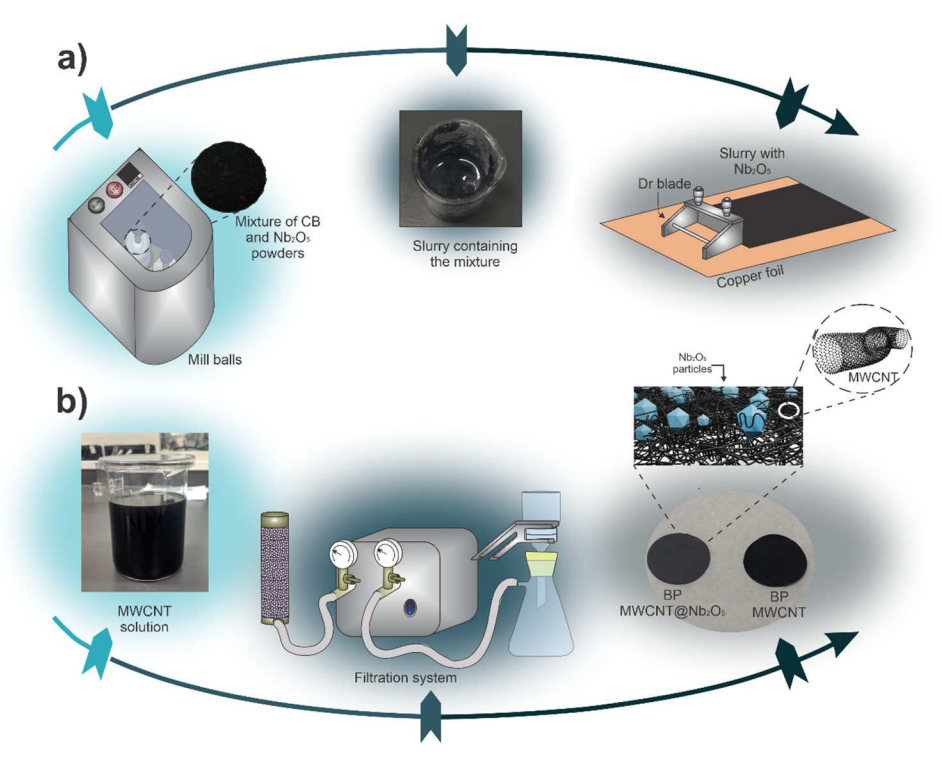


Fig. 1. Experimental set-up: (a) slurry or paint coating and (b) filtration for buckypaper techniques to develop the paint and buckypaper electrodes, respectively.

polar and non-polar parts, contributes to better dispersion [37]. These solutions were sonicated for 30 min to obtain a homogeneous dispersion and filtered slowly in a vacuum filtration with a pressure of 400 mmHg for approximately 4 h (Fig. 1b). For Nb₂O₅/MWCNT specimens, 20 mL of the precursor solution (MWCNT, DI and SDS) was retained and 3.0 mg of niobium pentoxide powder was added to it. This solution, previously ultrasonic treated, was also filtered to ensure that the Nb2O5 particles cover the surface of the carbon-based material. Lastly, 100 mL of deionized water was filtered through both materials to remove traces of surfactant and particles not strongly connected. Both buckypapers were removed from the filter and dried for 30 min at 80 °C on a hotplate, and then circular cells (10 mm) were cut from each buckypaper. Nb₂O₅/ MWCNT materials were inserted into a CVD furnace at 800 °C in an N₂ atmosphere at 5 °C minute⁻¹ for 1 h to guarantee the crystalline structure of the Nb₂O₅ and improve the contact between MWCNT and Nb₂O₅ nanoparticles. The mass of MWCNT and Nb2O5/MWCNT electrodes were $m \approx 1.8$ mg and 2 mg, respectively. The electrode thickness was approximately $\varepsilon \approx 80 \ \mu m$.

2.4. Surface and structural characterizations

The surface morphology of composite electrodes was examined at different magnitudes using a FEI Nova NanoSEM450 equipped with Everhart–Thornley (ETD), Through the Lens (TLD) and energy-dispersive (EDS) detectors applying 5 kV and spot 5.0. In addition, a JeoL MSC2100 transmission electron microscope (TEM) with 300 kV was used to obtain high-resolution images, and TEM data were analyzed using ImageJ software to estimate particle size and distribution.

The crystalline structure was characterized via XRD with an X'Pert-MPD from Philips Analytical, using Cu-K α radiation ($\lambda=1.54056$ Å Almelo, Netherlands). The diffraction patterns were collected with steps of 0.02° and the accumulation time of 0.6 s per step within the range of $10^{\circ}–90^{\circ}(20\text{-scale})$. The General Structure Analysis System (GSAS) program [38] suite with the EXPGUI interface [39] was used to perform a Rietveld refinement [24] to identify the crystal phase. The original Rietveld formulation and others successors of its [40] represented the diffraction line width in a smooth function of the d-spacing from the

diffraction angle (20, considering that some peaks of interest near 20 presented different widths). Accordingly, this work used the peak profile function developed by Stephens et al. [41] to conduct the experimental data. By this method, diffraction widths which are not a smooth function of d are performed, resulting from anisotropic sample size broadening or from a particular pattern of defects (e.g., stacking faults). In order to consider this anisotropy in the half-width of the reflections, the bidimensional model for crystallite size described by Larson & Von Dreele [38] was used.

The crystalline phase was identified using the International Center for Diffraction Data (ICDD) catalogue, and the following equation was used to correct line broadening for the instrumental effects:

$$\beta = \sqrt{\beta_{Exp}^2 - \beta_{Standard}^2},\tag{1}$$

where β is the full width at half-maximum (FWHM) of the peak. $B_{Standard}$ was obtained from standard LaB₆ powder (SRM660-National Institute of Standard Technology) using the Caglioti equation [42]:

$$\beta_{Standard} = \sqrt{u \tan \theta^2 + v \tan \theta + w},\tag{2}$$

Electron density maps were calculated according to a previous method [41]. In brief, a point (x, y, z) of the crystallite cell with volume (V) was calculated using the Fourier series and the structural factors F(h, k, l):

$$\rho(x, y, z) = V^{-1} \sum_{h} \sum_{k} \sum_{l} F(h, k, l) exp[2\pi i (hx, ky, lz)]$$
 (3)

where (x, y, z) represents a vector (r) of real space, with one vector space (a, b, c) and another vector (h, k, l) that represent the coordinates of one vector from the reciprocal space with base (a^*, b^*, c^*) (i.e., coordinates from the diffraction plane given by Bragg's Law). Electron density distribution in the plane {slice 1 with x = y = z = 1 (i.e., face abc), with a set (hkl) as the projection plane (100) & (101) for monoclinic crystallography phase and (001) & (100) for orthorhombic crystallographic phase} was calculated.

The surface chemistry and valences states were examined via X-ray

photoelectron spectroscopy (XPS) from Thermo Scientific, with monochromatic Al anode K α (h $\nu=1486.6$ eV), spot size 400 μ m. Raman spectroscopy was performed using a Renishaw inVia Raman spectrometer with a 633 nm excitation laser. Spectra were measured at room temperature using a 50× Laser Direct Writing (LDW) objective lens in the range of 100–3200 cm $^{-1}$. The Raman shift was calibrated using a standard silicon sample with peak position of 520.5 cm $^{-1}$.

2.5. Electrochemical characterization of the symmetric supercapacitor and half-cell battery

The electrochemical behavior of the electrodes containing Nb_2O_5 was studied both as sodium-ion symmetric supercapacitor (SIC or NIC) and sodium-ion battery (SIB or NIB). The paint electrode was tested only as a working electrode in a half-cell configuration in order to assess the electrochemical contribution of Nb_2O_5 . While the $Nb_2O_5/MWCNT$ electrode was evaluate as both a working electrode in a half-cell battery and in a full cell symmetric supercapacitor. In the same way, the neat MWCNT electrode was evaluated to compare the performance with $Nb_2O_5/MWCNT$ electrode in order to better estimate the contributions of Nb_2O_5 .

All experiments were carried out at 24 $^{\circ}\text{C}$ using a model CR2032 coin cell in the two-electrode configuration soaked with 90 μL of 1 M NaClO₄ in EC:DMC (1,1 $\nu/\nu)$. A sodium metallic (reference) and a Celgard separator were used to assemble the battery cells. Two identical electrodes (symmetric model) and a cellulose separator (NKK TF4850) were employed for supercapacitor cells. The electrodes and separators were put into a vacuum oven at 80 $^{\circ}\text{C}$ overnight, and the devices were assembled in an argon-filled MBraun Labmaster SP/DP glove box.

Electrochemical characterization of the SIC coin cells was initiated using the cyclic voltammetry (CV) technique in the voltage range of 0 - $U_{\rm vertex}$ (e.g., $U_{\rm vertex}=2.0, 2.2, 2.4, 2.6, 2.8, 3.0,$ and 3.2 V) at 5.0 mV s $^{-1}$. Also, galvanostatic charge-discharge (GCD) experiments were accomplished at 0.05, 0.1, 0.2, 0.5, 1, 2, 5, and 10 A g $^{-1}$ using the same voltage range as the CV experiments. Cell-aging analysis was performed via successive GCD with a current of 10 A g $^{-1}$ until 10,000 cycles.

EIS spectra for the SIC coin cells were registered at $U=3.0~\rm V$ for both MWCNT and Nb₂O₅/MWCNT nanostructured materials. The frequency range of 100 kHz to 10 mHz was swept by a small sinusoidal signal of 10 mV (peak-to-peak) to linearize the impedance response. Accurate simulations of the impedance data using the TL model were obtained with a relative error less than 5% for each model's parameter. Kramers-Krönig tests, characterized by low chi-square values (ca. $\chi^2 < 10^{-4}$), were accomplished to validate the impedance data. Theoretical analysis of the impedance data was performed using the well-known two-channel TL model proposed by proposed by Bisquert [31,43].

The specific capacitance from CV was calculated from the following equations:

$$q = \frac{1}{v} \int_{U_i}^{U_f} I \, dU, \tag{4}$$

where U_f and U_i are the initial and final voltages during the scan process, respectively.

$$C_{specific} = \frac{q}{m\Delta U},\tag{5}$$

where m is the mass of the material presents on both electrodes and $\Delta U = |U_f - U_i|$ is the voltage window.

The maximum specific capacitance of a device, $C_{\rm max}$, is obtained from the GCD experiments applying the minimum current necessary to charge it in attempt to minimized ohmic losses. The following Equation was used to calculate it:

$$C_{\text{max}} = \frac{I_{\text{min}}}{m(\frac{dU}{dt})},\tag{6}$$

where $I_{\rm min}$ is the minimum discharge (cathodic) current, m is the mass of MWCNT or Nb₂O₅/MWCNT nanostructured materials, and dU/dt is the derivative of the discharge curve.

Hence, the specific energy (E) and power (P) can be calculated using the following equations [4]:

$$E_{\text{max}} = \frac{C_{\text{max}}U_{\text{c}}^2}{2},\tag{7}$$

$$P_{\text{max}} = \frac{U_{\text{c}}^2}{4R_{\text{c}}},\tag{8}$$

where $U_{\rm c}$ is the total voltage drop referring to the equivalent series resistance (ESR), and $R_{\rm S}$ is the solution (ionic) resistance obtained from EIS spectra.

To display the Ragone plot, a numerical solution in function of the energy and the power was proposed by Vicentini et al. and Silva et al. [4,44]:

$$E_L = \frac{E_{\text{max}}}{2} \left(1 + \sqrt{1 - \frac{P_L}{P_{\text{max}}}} \right),\tag{9}$$

where $E_{\rm L}$ and $P_{\rm L}$ are the load energy and power, respectively.

The coulombic efficiency (η) is obtained from the ratio measured in the discharging and charging GCD experiments [1]:

$$\eta = \frac{q_{\text{discharging}}}{q_{\text{charging}}} \times 100\%, \tag{10}$$

Otherwise, the electrochemical performance of the battery cell consists of GCD at gravimetric current of $25~\text{mA}~\text{g}^{-1}$ at 2.25~V until 100 cycles. According to Glaize et al., the capacity is related to the amount of charge released by a cell, active material, or an electrode [45]. Therefore, the specific capacity for the charge-storage process can be measured from the following equation [45]:

$$C_{esp} = \frac{I_t}{m} \int_0^t dt, \tag{11}$$

where I_t is the current applied, dt is the time while the cell voltage range and m the active mass of the electrode.

Whole electrochemical experiments were conducted using the BCS-810 cycler equipment from Bio-Logic Science Instruments.

3. Results and discussion

3.1. Morphological and structural materials characterization

The surface morphology and structure analyzed by SEM is shown in Fig. 2 for all electrode materials with different magnitudes. The $\mathrm{Nb}_2\mathrm{O}_5$ nanoparticles and Carbon Black coating images on the copper foil (Fig. 2a–c) exhibited a thin layer composed of tiny particles equally distributed. The micrographs showed homogeneous particle distributions and no charging issue during SEM analyses, meaning that the carbon black works perfectly as an electron extractor, indicating a continuous conductive path. Fig. 2d–f shows the micrographs from the buckypapers, revealing an entangled, spaghetti-like distribution. The buckypaper with $\mathrm{Nb}_2\mathrm{O}_5$ nanoparticles (Fig. 2g–i) also showed a random particle distribution covering the surface surrounded by the MWCNTs, as observed in Fig. 2h, allowing the carbon material to work as a current drain for $\mathrm{Nb}_2\mathrm{O}_5$ nanoparticles. ImageJ software was used to measure nanoparticle size, ranging from 40 to 100 nm (Fig. 2i).

Fig. 2j–l shows structural micrographs of the $Nb_2O_5/MWCNT$ nanostructured materials. TEM confirmed that the MWCNTs had diameters of approximately 20 nm with a tubestratic structure, while the Nb_2O_5 nanoparticles presented a crystalline material randomly dispersed and wrapped by MWCNT. Fig. 2l shows that the niobium pentoxide was polycrystalline (please see below discussion regarding

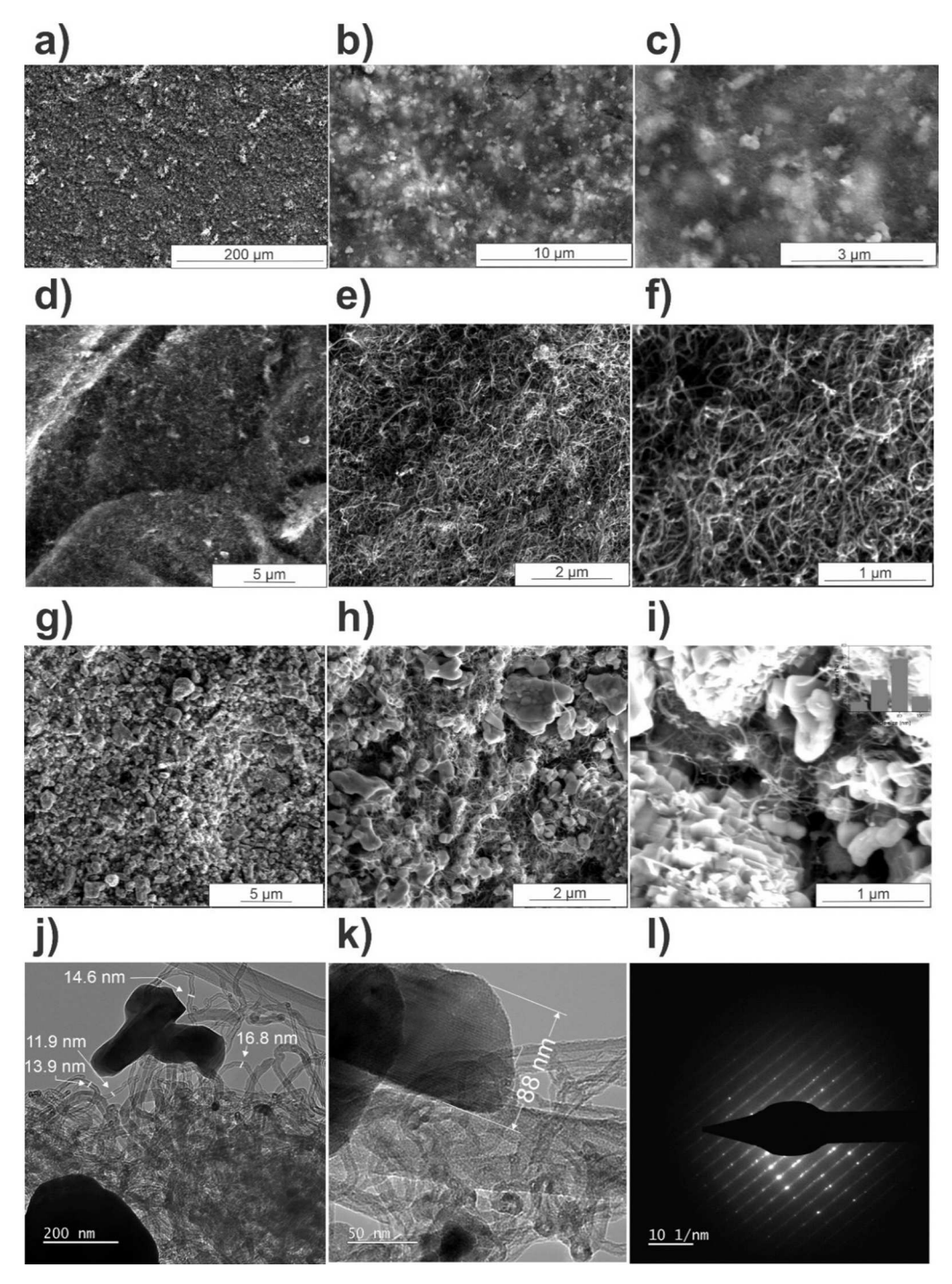


Fig. 2. Scanning Electron Microscopy with different magnitudes (a–c) $1000\times$, $20,000\times$ and $60,000\times$ from Nb₂O₅ coating on copper foil and $5000\times$, $20,000\times$ and $100,000\times$ from buckypapers (d–f) MWCNT, (g–i) MWCNT/Nb₂O₅ and (j) Transmission Electron Microscopy (k) High-Resolution Transmission Electron Microscopy and (l) selected area electron diffraction from MWCNT/Nb₂O₅.

XRD data).

Fig. 3a shows the Raman spectra of i) MWCNT, ii) Nb₂O₅ nanoparticles, and iii) Nb₂O₅/MWCNT nanostructured materials, which is a combination of i) and ii), respectively. The results agreed with the SEM images, indicating that the Nb₂O₅ is readily available at the electrode surface. Results analysis deconvoluted the spectra to identify Raman resonant modes are presented in Fig. S1 from Supplementary information, Section II.

Raman spectrum from MWCNT is well known [46]. The current study identified D, G, D', and 2D bands at 1326, 1576, 1610, and 2643 $\,\mathrm{cm}^{-1}$, respectively, and two less intense bands at 1154 and 1477 $\,\mathrm{cm}^{-1}$

from the MWCNT Raman spectrum. The G band was assigned to the $\rm E_{2g}$ phonon at the Brillouin zone centre due to the iLO and iTO phonon branches [47]. Additionally, the D and D' bands, which involve an intervalley and intravalley double resonance process, respectively, are related to the transverse optical phonon due to the Kohn anomaly around the K-point, revealing defects to the breathing modes of six atom rings generally concentrated at the crystalline edges or boundaries [48,49]. The less-intense bands at 1154 and 1477 cm $^{-1}$ were assigned to the amorphous like-carbon (e.g., defect short carbon layers) and oxygen functional groups [37,50–53]. The 2D band was the second harmonic of the D band, but no defects were required for their activation [48].

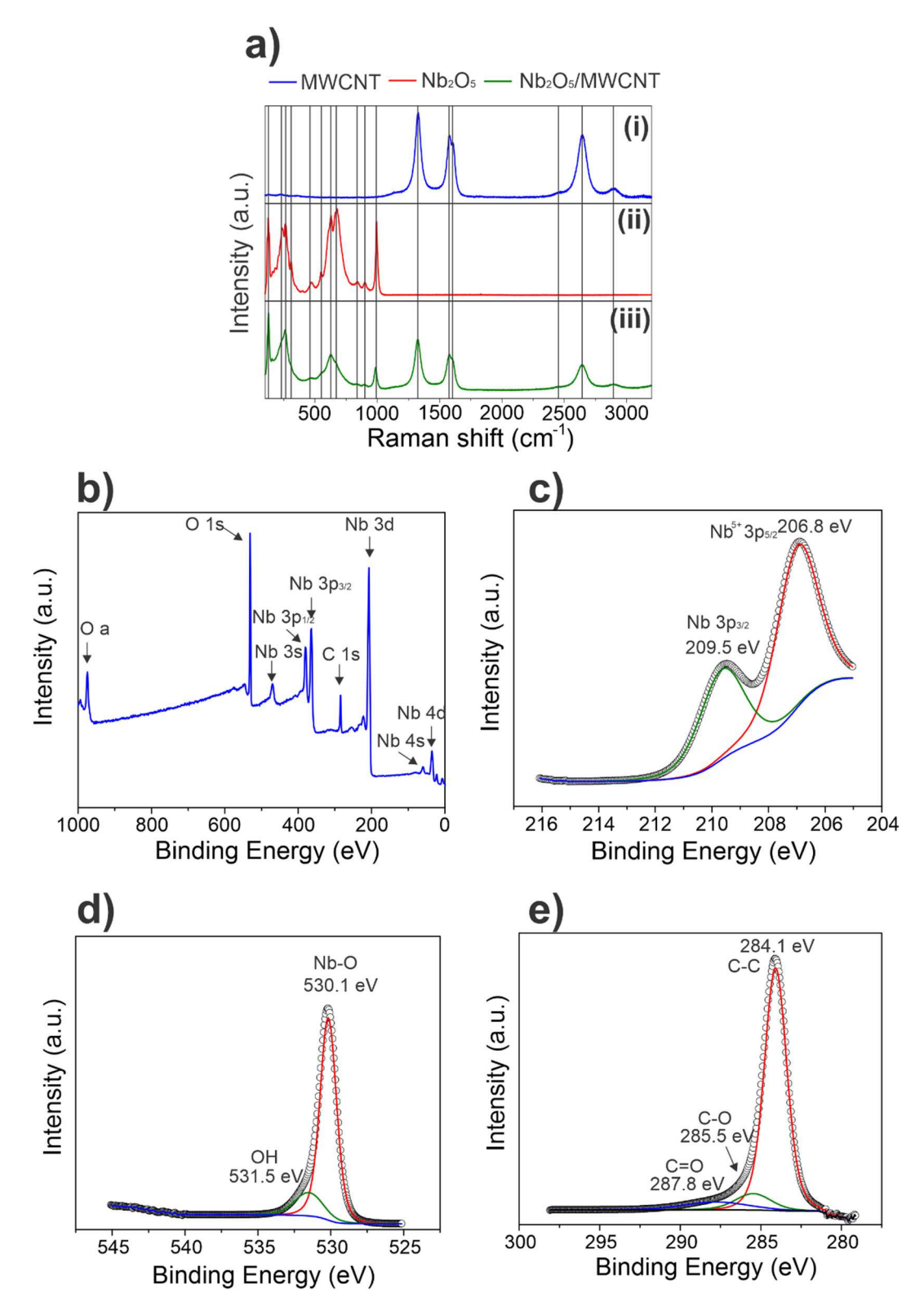


Fig. 3. (a) Raman spectra of MWCNT (blue), Nb_2O_5 (red) and Nb_2O_5 /MWCNT (green); (b) XPS Survey spectrum (c-e) high resolution XPS spectra of (c) Nb 3d, (d) O 1s and (e) C 1s for the buckypaper Nb_2O_5 /MWCNT. (For interpretation of the references to colour in this figure legend, the reader is referred to the web version of this article.)

For the $\mathrm{Nb_2O_5}$ nanoparticles, the contrasted bands were 123, 173, 206, 234, 265, 285, 309, 470, 547, 605, 627, 676, 901, and 993 cm⁻¹, which is similar to previous works [15,16]. Niobium oxides were primarily assigned to bands between 800 cm⁻¹ and 1000 cm⁻¹ (ν_I) due to A1 type longitudinal optic modes corresponding to the symmetrical

metal-oxygen stretching vibration on octahedral structure [16,54]. However, bands appearing at 605–676 cm⁻¹ (ν_2) corresponded to the transverse optic modes [54]. Bands at 123–173 cm⁻¹ were assigned to the external modes, while bands in the range of 206–309 cm⁻¹ to the triple degenerated vibration mode in the T_{3u} region [15,16]. The band at

234 cm⁻¹ corresponded to bending modes of Nb-O-Nb bonds, known as v_6 (T_{2u}) mode. Furthermore, the band at 470 cm⁻¹ was designated to the T_{2g} region, and the band at 839 was assigned to Nb-O-Nb colinear bonds of the corner-shared NbO₆ [54,55]. Bands at 901 and 993 cm⁻¹ were attributed to the symmetric and antisymmetric Nb=O stretching modes of the terminal bonds, respectively [54,55]. The niobium pentoxide data showed orthorhombic and monoclinic phases [55].

XPS measurements from the MWCNT and Nb_2O_5 nanoparticles are presented in Fig. 3b–e, the survey spectrum, and the high-resolution spectra of Nb 3d, O 1s, and C 1s, respectively. The XPS survey spectrum revealed the presence of Nb, O, and C elements. High-resolution spectrum of Nb 3d indicated two intense peaks at 209.5 eV and 206.8 eV, which corresponded to binding energies for Nb 3d3/2 and Nb 3d5/2, respectively, as is characteristic of the Nb^{5+} [15,16,55]. The O 1s spectrum revealed two-component peaks. One peak, located at 530.1 eV, was assigned to the O^{2-} coinciding with the ion in the Nb_2O_5 species, and the other peak, located at 531.5 eV, was related to the hydroxyl group absorbed for the MWCNT film [15,16]. The three-component peaks presented in the C 1s spectra at 284.1, 285.5, and 287.8 eV were associated with non-oxygenated ring carbon (C—C), C—O bonded carbon, and C—O carboxylate carbon [15,16,57].

The structural properties of Nb₂O₅/MWCNT nanostructured materials were studied by XRD and Rietveld refinement, as presented in Fig. 4. Also, Cartesian coordinates of H-Nb₂O₅ and T-Nb₂O₅ crystalline phases calculated were presented in Supplementary Section III. As observed, XRD patterns showed the Nb2O5 prominent reflections at 22.6068 (0 0 1)-hkl plane, 28.3999 (1 8 0)-hkl plane, 28.4702 (1 8 0)-hkl plane, 36.5249 (1 8 1)-hkl plane and 37.0909 (2 0 1)-hkl plane which was related to Nb₂O₅ - orthorhombic crystalline phase (Nb₂O₅ - CIF ICSD 1840). Furthermore, reflections at 23.7252 (1 1 0)-hkl plane, 24.4946 (1 $0\ \overline{5}$)-hkl plane, 25.5470 (6 0 $\overline{2}$)-hkl plane, 31.5770 (5 $\overline{1}\ \overline{2}$)-hkl plane, 32.2037 (5 1 1)-hkl plane, 33.1097 (2 1 5)-hkl plane, 35.2423 (5 0 3)-hkl plane, 36.0320 (7 0 7)-hkl plane, 38.8819 (6 1 6)-hkl plane, 43.4579 (10 $(0.5)^{-1}$ plane, 44.5506 $(2.0.5)^{-1}$ plane and 47.4693 $(0.2.0)^{-1}$ plane were observed and related to Nb₂O₅ - monoclinic crystalline phase (Nb₂O₅ - CIF ICSD 29). The structural and statistical parameters related to the Rietveld refinement presented in Fig. 4a can be observed in

 $\begin{tabular}{ll} \textbf{Table 1} \\ \textbf{Structural} \ \ \text{and} \ \ \text{statistical parameters} \ \ \text{using Rietveld refinement for Nb}_2O_5/MWCNT \ \ \text{nanostructured materials}. \\ \end{tabular}$

Parameters/phase	Orthorhombic/T-Nb ₂ O ₅	Monoclinic/H-Nb ₂ O ₅
a/Å	6.16954 (2)	21.19473 (1)
b/Å	29.27970 (9)	3.82755 (0)
c/Å	3.93517 (1)	19.31736 (9)
α/degrees	90	90
β/degrees	90	119.83 (3)
γ/degrees	90	90
V/Å ³	710.85 (9)	1359.43 (1)
Particle size/nm	70.0	52.0
Lattice strain/%	0.205	0.317
Wt. Fraction	0.61820	0.38180
χ^2	1.401	
R (F**2)	0.1199	
w <i>R</i> p	0.2285	
Rp	0.1738	

Table 1. The acceptance of the structural refinement data is possible if two cases are satisfied: (i) the weighted index $(R_{\rm wp})$ is $R_{\rm wp} < 10\%$ [24] and (ii) the variance between the observed values and the values expected under the model in question (χ^2) is lower than two [24]. Thus, it was possible to infer that the Rietveld refinement evaluated for the Nb₂O₅/MWCNT nanostructured materials agreed with the Rietveld proceedings.

As showed in Table 1, lattice parameter (a,b,c,α,β) and γ) were in agreement with those values obtained for file card CIF ICSD 1840 for Nb₂O₅ - orthorhombic crystalline phase (space group Pbam, a=6.175 (1) Å, b=29.175(4) Å, c=3.930(1) Å, $\alpha=\beta=\gamma=90^\circ$) and file card ICSD 29 for Nb₂O₅ - monoclinic crystalline phase (space group P12/m1 a=21.153(7) Å, b=3.8233(5) Å, c=19.3560(50) Å, $\alpha=\gamma=90^\circ$ and $\beta=119.80$ (2)°). Furthermore, particle size and lattice strain were evaluated as described below.

The constant wavelength profile implemented into GSAS routine uses a pseudo-Voigt convolution and asymmetry function, as well, the microstrain broadening description of Stephens et al. [41]. The Gaussian variance of the peak, $\sigma 2$, modifies with 2θ as:

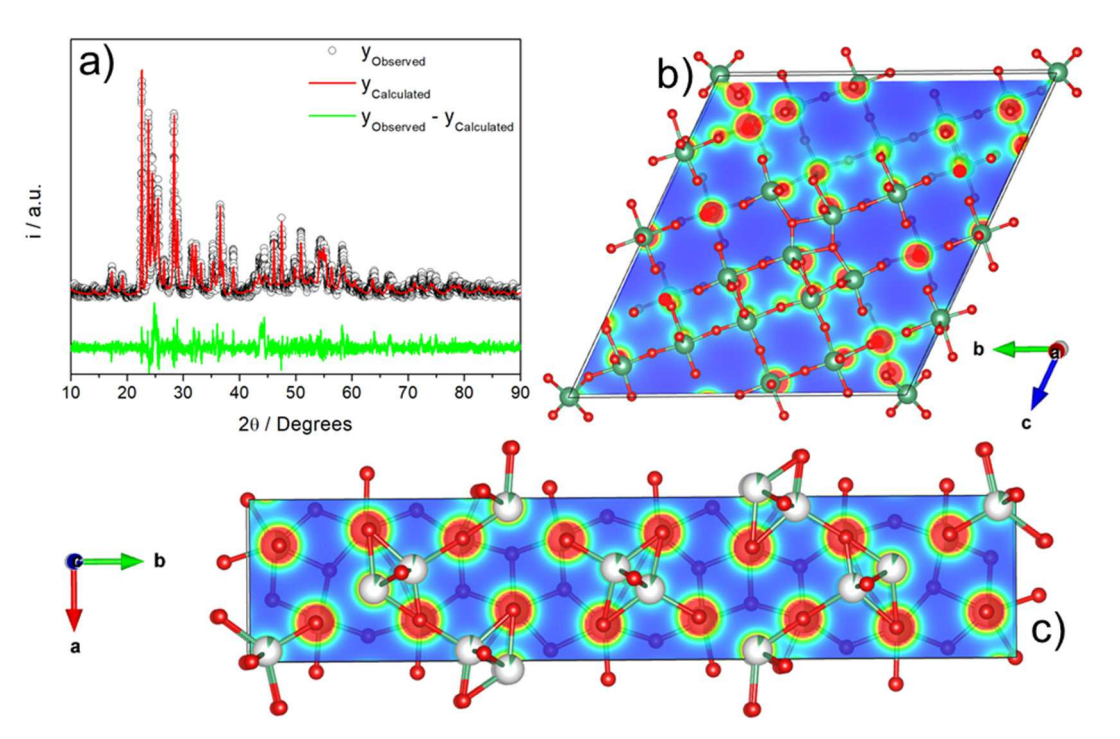


Fig. 4. (a) Rietveld refinement pattern and electron density maps for (b) (101) H-Nb₂O₅ and (c) (001) T-Nb₂O₅ crystalline phases.

$$\sigma^{2} = \left(U + \sigma_{S}^{2} d^{4}\right) \tan^{2}\theta + V \tan\theta + W + P/\cos^{2}\theta, \tag{12}$$

where *U*, *V* and *W* are the coefficients described by Caglioti et al. [42] and *P* is the Scherrer coefficient for Gaussian broadening. Therefore, the particle size broadening can be calculated from:

$$\Delta d/_{d^2} = \frac{\Delta 2\theta cot\theta}{d} = constant, \tag{13}$$

From Bragg's law then:

$$\Delta d/_{d^2} = \frac{2\Delta 2\theta cot\theta sin\theta}{\lambda},\tag{14}$$

The broadening is:

$$\Delta 2\theta = \frac{\lambda \Delta d_{d}}{2\cos\theta},\tag{15}$$

Considering that, the first term of Eq. (15), related to the Lorentzian broadening, is expressed from:

$$X = \frac{\Delta d}{d^2},\tag{16}$$

Therefore, the particle size can be determinate rearranging Eq. (15) with Eq. (16), and converting from centideg to radians from:

$$p = \frac{18000K\lambda}{\pi X},\tag{17}$$

where *K* is the Scherrer constant.

It is possible to notice in Table 1, particle size of 70 nm and 52 nm for Nb₂O₅ orthorhombic and monoclinic crystalline phases, respectively. Mohallem et al. [58] studied the phase transition employing strain mapping in TT-, T- and H-Nb₂O₅ nanoparticles obtained using the polymeric precursor method. Moreover, the authors also performed Rietveld refinement for whole samples obtained. According to the authors [58], T-Nb₂O₅ nanoparticles presented a=6.165(1) Å, b=29.253 (9) Å and c=3.928(1) Å, while H-Nb₂O₅ nanoparticles presented a=20.959(4) Å, b=3.827(7) Å, c=19.308(5) Å and $\beta=119.06^{\circ}$. The authors also obtained 62 nm and 83 nm particle sizes for T- and H-Nb₂O₅ nanoparticles, respectively. Particle sizes varying from 33.8 nm up to 45 nm were also presented in the literature. However, the authors have not qualitatively described between T- and H-Nb₂O₅ crystalline phases. As a result, the lattice parameter and crystallite size presented herein agree with the literature.

Still analyzing constant wavelength experiments, the strain broadening in real space is related to 2θ broadening from:

$$\Delta d/_{d} = \Delta 2\theta \cot\theta = constant, \tag{18}$$

In this expression, $\Delta 2\theta$ is in radians. Examinating the expression for the Gaussian broadening:

$$\sigma^2 = U tan^2 \theta + V tan \theta + W + P/\cos^2 \theta, \tag{19}$$

shows that the first term contains a strain broadening element. Consequently, the variation and the instrument contribution can be subtracted off. This variation (centideg²) must be converted to radians aiming to yield strain:

$$S = \frac{\pi}{18000} \sqrt{(8ln^2)(U - U_i)} *100\%, \tag{20}$$

This research methodology was used to calculate T- and H-Nb₂O₅ lattice strain (Table 1). As presented in the table, T-Nb₂O₅ and H-Nb₂O₅ showed 0.205% and 0.317%, respectively, as compared to Mohallem et al. [58] who obtained 0.370% and 0.107% for TT-Nb₂O₅ and T-Nb₂O₅ nanoparticles, respectively. Surprisingly, H-Nb₂O₅ nanoparticles presented 0%. Halbos et al. [59] studied the hydrothermal preparation of Nb₂O₅ nanoflakes as a function of deposition time. The authors obtained 0.309% average lattice strain for Nb₂O₅ nanoflake samples. However,

any distinction between several $\mathrm{Nb_2O_5}$ crystalline phases was performed.

Tensile and compressive strain are two types of stresses a material commonly experiences. A strain can be defined as any deformation of an object measured geometrically related of a fraction of some original value. Therefore, tensile strain is known as the fractional increase in length of an object submitted to tensile stress, whereas a compressive strain is the fractional decrease in length of an object submitted to compressive stress. Consequently, the lattice parameter obtained for T-and H-Nb₂O₅ crystalline phases was compared to related ICSD #1840 (T-Nb₂O₅) and ICSD #29 (H-Nb₂O₅). Results showed a tensile strain preferred oriented along the b-axis and a-axis for T-Nb₂O₅ and H-Nb₂O₅, respectively. The control of lattice strain is pivotal for tunning structural properties related to the presence of channels into crystalline phases, such as the intercalation/de-intercalation process and numerically modelling EIS data using TL models.

The control and tunning properties of a channel within a nanostructured system significantly impact the reversible capacity and cyclability of ESDs. The low reversible capacity and poor cyclability for Na⁺-ion batteries compared to Li⁺-ion batteries, especially at high current rates, are related to the larger Na⁺-ion (1.02 Å) compared to the Li⁺ion (0.76 Å), which causes a large volume change and irreversible phase transition during Na+-ion intercalation/de-intercalation processes. Wang et al. [60] studied Na⁺-ion diffusion into graphite structures and found that the insertion of the Na+-ion into graphite is substantially hindered by insufficient interlayer spacing. As a result, they suggested a new synthesis route to enlarge the distance of the interlayer lattices to 4.3 Å for modified graphite structures. Similarly, Liu et al. [61] used the density functional theory (DFT) to determine that the interlayer distance of graphite (\sim 3. 4 Å) is too small to accommodate the large Na⁺-ion, and a minimum interlayer distance of 3.7 Å is required for Na⁺-ion insertion. For graphite with an interlayer spacing of 3.35 Å, the energy cost for Li⁺ion insertion is 0.03 eV, while for Na⁺-ion insertion, the energy cost is 0.12 eV. Willmann et al. [62] obtained these same results when they observed that the equilibrium interplanar distance for NaC₆ is approximately 4.5 Å and 3.7 Å for LiC₆.

Fig. 4b–c presents diffusion channels as suggested by theoretical calculation and experimental observation. Fig. 4b presents an oriented (101) H-Nb₂O₅ crystalline phase, and Fig. 4c shows a (001) T-Nb₂O₅ crystalline phase. The lattice parameters were $d_{(101)}$ H-Nb₂O₅ = 3.820 Å and $d_{(001)}$ T-Nb₂O₅ = 3.950 Å, respectively. In addition, Fig. 4b–c identifies the lowest electron density charge as blue, while the atomic positions with the highest electron density charge are red. Abreu et al. [63] studied the structural, electronic, and thermodynamic properties of the T and B phases of Nb₂O₅ using DFT and the electron localization function (ELF). They obtained an ELF map in the (001) direction in the T-Nb₂O₅ crystalline phase and a similar absence of charge as presented in Fig. 4c.

Finally, Table 1 compares the considerable weight fraction of the T-Nb₂O₅ crystalline phase (61.82%) and the H-Nb₂O₅ crystalline phase (38.18%), which explains the improved ESD performance when $d_{(001)}$ T-Nb₂O₅ > $d_{(001)}$ H-Nb₂O₅. The higher weight fraction and larger lattice parameter for the T-Nb₂O₅ crystalline phase was related to the TL impedance models displayed by Nb₂O₅/MWCNT nanostructured materials. The Rietveld result was in agreement with the distribution Gaussian obtained from SEM results presented in Fig. 2i. A particle size range of 40–100 nm was also observed, and ~60% of the particles presented large sizes between 70 and 100 nm.

3.2. Electrochemical performances

3.2.1. Na⁺-ion pseudocapacitor properties

Electrochemical data from the symmetric coin cell device containing MWCNT and $Nb_2O_5/MWCNT$ nanostructure materials are presented in Fig. 5. For a fair comparison, the electrochemical results were obtained from the entire electrodes' mass. Moreover, the cell voltage was studied

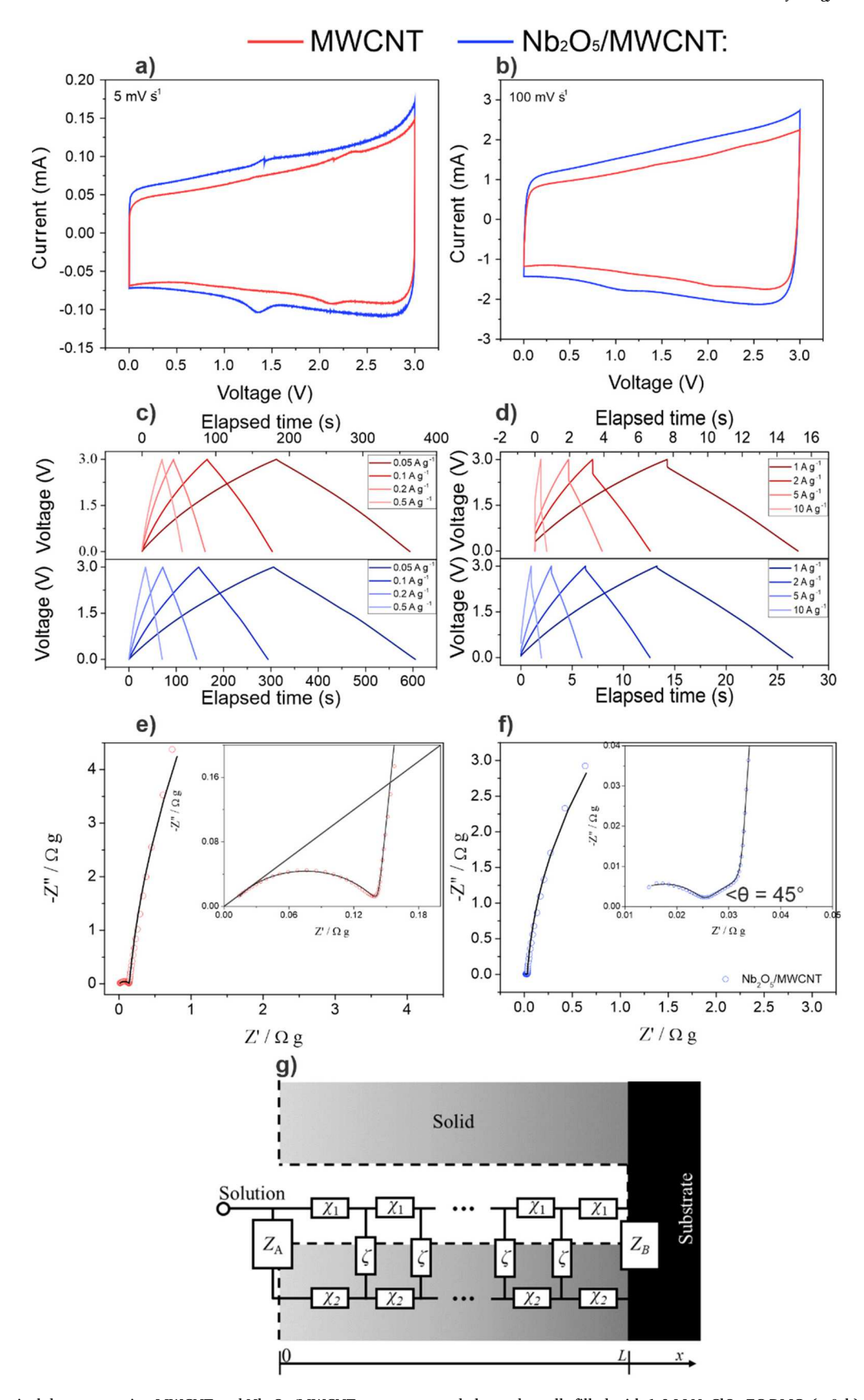


Fig. 5. Electrochemical data comparing MWCNT and Nb₂O₅/MWCNT nanostructured electrodes cells filled with 1.0 M NaClO₄ EC:DMC. (a & b) cyclic voltammetry at 5.0 mV s⁻¹ and 100 mVs⁻¹, respectively, (c & d) galvanostatic charge-discharge curves with different currents (0.05 A g⁻¹, 0.1 A g⁻¹, 0.2 A g⁻¹, 0.5 A g⁻¹, 1.0 A g⁻¹, 2.0 A g⁻¹, 5.0 A g⁻¹ and 10 A g⁻¹), (e & f) Nyquist spectra at U = 3.0 V and (g) two-channel transmission line impedance model: $\chi_1 = r_{\text{Pore}}$, $\chi_2 r_{\text{Material}} = \text{and } \zeta = r_{\text{ct}}q_{\text{dl}}$.

to establish the electrochemical stability of the presented system and avoid electrolyte decomposition and misinterpretation of cell data. A systematic study of cell voltage related to cyclic voltammetry, gravimetric chronoamperometry, electrochemical impedance spectroscopy, and galvanostatic charge-discharge from 0 V up to $U_{\rm Vertex} = 2.0, 2.2, 2.4, 2.6, 2.8, 3.0,$ and 3.2 V is presented in Supplementary information on Section IV (Figs. S2 and S3).

Fig. 5 also shows that the electrochemical performance of the symmetric coin cell device with MWCNT and Nb₂O₅/MWCNT nanostructured materials ranged from 0 to $U_{\rm vertex}=3.0$ V when watersplitting was not present. In all cases, nearly rectangular capacitive voltammetric curves were expected for electrical double-layer capacitors. Surprisingly, the Nb₂O₅/MWCNT nanostructured electrodes presented a redox process near 1.3 V along cathodic and anodic sweeps under a low scan rate (e.g., 5.0 mV s⁻¹) related to pseudocapacitive materials. This peak corresponds to the redox couple of Nb⁴⁺/Nb³⁺ [64] and matches Reaction (1) [65]. Otherwise, the MWCNT electrodes presented a less intense redox process near 2.0 V. This can be explained by the fact that MWCNT shows some functional groups and catalyst impurities (please, EDS data Table S5 in the Supplementary information Section V).

The charge-storage mechanisms of pseudocapacitive materials are reasoned on redox reactions and on electrical double-layer charge storage presented by capacitive materials, showing an electrochemical response similar to capacitors. The capacitance, C (F g^{-1}), can be obtained as a function of the potential, $V(C = QV^{-1})$. Then, a linear increase of the stored charge, Q, with the rise in the potential is expected for pseudocapacitive materials. This nearly linear dependence of the storage charge within the potential window indicates that the faradaic charge storage is not limited by diffusion, a characteristic feature of a pseudocapacitive material. The energy stored in a pseudocapacitive material can be calculated by $E = 0.5CV^2 = 0.5QV$. Differently, a battery material reveals a defined voltage plateau. Accordingly, most of the charge is stored at a constant potential. The energy stored in a battery material is obtained by E = QV when an incremental charge is inserted at a constant potential. Therefore, Nb₂O₅/MWCNT nanostructured materials presented pseudocapacitor, which is characteristic of intercalation processes. Similarly, the literature describes H-Nb₂O₅ [66-68] and T-Nb₂O₅ [69-71] crystalline phases for electrical double-layer, pseudocapacitor, and battery applications.

Fig. 5c–d presents galvanostatic charge/discharge data in triangular shapes for all currents (0.05, 0.1, 0.2, 0.5, 1, 2, 5, 10 A g $^{-1}$) studied. The addition of Nb $_2$ O $_5$ nanoparticles onto the MWCNT nanostructured matrix did not impact the equivalent series resistance (ESR) of the cell. The ESR values were $14.2\pm0.1~\text{m}\Omega$ g and $17.7\pm0.1~\text{m}\Omega$ g for MWCNT and Nb $_2$ O $_5$ /MWCNT nanostructured electrodes, respectively.

As mentioned, most EIS studies of supercapacitors are reasoned on inadequate equivalent circuit analogs, resulting, commonly, in satisfactory statistics for the simulation/fitting process but not providing a rational correspondence to the fundamental physicochemical processes that occur during the charge-discharge processes, especially for porous materials. Therefore, the current study investigated the EIS technique using the TL approach, which has rational physicochemical support. The diffusion impedance and recombination or diffusion and coupled reaction were modelled as a finite-length TL, in which the complex plane plot of this impedance showed a straight line with 45° at high frequency and then ascended vertically at the low frequency. Therefore, a TL model was expected once the system presented an appropriated lattice spacing parameter, as shown in Figs. 2l and 4b–c, respectively.

De Levie [27,28] initially proposed the canonic models for porous electrodes under various polarization conditions with an assembly of evenly distributed identical cylindrical pores. The ionic and electronic phases in intimate contact were ideal conductors. As an improvement to De Levie's work, various authors have proposed more elaborated porous electrode models. For example, impedance models developed by Bisquert et al. [30,72] considered the influence of anomalous transport

processes for the ionic and electronic phases in intimate contact, which are of particular relevance for the study of energy storage materials with porous and disorder characteristics.

Overall, the Nyquist plot verified in Fig. 5e-f was marked by two arcs distributed in the low- and high-frequency ranges and a significant decrease (orders) in the resistance values for Nb2O5/MWCNT nanostructured electrodes compared to MWCNT nanostructured electrodes. However, an increase in the real part impedance extrapolation of the low-frequency semicircle was noticed. This decrease could be associated to the Nb₂O₅ nanoparticles homogeneously dispersed into the Nb₂O₅/ MWCNT nanostructured electrode, as shown in Fig. 2. Furthermore, the complex plane plot of MWCNT and Nb₂O₅/MWCNT nanostructured electrode impedance shifted into a straight line with 45° at high frequency. This profile will be keen discussed further in the development of the TL model to obtain numerically modelled electrochemical impedance parameters. The porous electrode model theoretically predicted this impedance profile, which incorporated transport anomalies and was represented by a two-channel TL. The current study used the TL model shown in Fig. 5g to model the impedance findings, resulting in accurate statistics numerically, as presented in Table 2 (e.g., validated F, t-tests,

The configuration assumed in our model suggested in Fig. 5g consists of a porous electroactive thin film deposited on a conducting substrate and flooded with an electrolyte. Thus, the electrode region is considered a mixture of two phases that conduct different electronic and ionic species. The macroscopic boundaries are impermeable to other species [73]. It is supposed that the ionic species in the pores dipped in the electrolyte can be exchanged freely with the bulk solution at the pore's entry (x=0), as well the electronic charge carrier in the solid phase can also be withdrawn or injected freely at the contact with the substrate (x=L;L) is the electrode layer thickness). Faradaic currents and polarization may happen at the inner surface separating the two phases.

The impedance model is developed using the equations describing the local variation of electric current and potential in each phase [72] and is demonstrated in the Supplementary information (Section VI).

The numerical modelling parameters obtained with two-channel TL (Supplementary information - Section VI) are presented in Table 2. It is possible to notice similar electrolyte resistance values independent of electrode nature. The ESR values obtained from GCD and discussed previously in Fig. 5c, d agree with pore resistance with 16% deviation for both MWCNT and Nb2O5/MWCNT nanostructured electrodes. The presence of MWCNT as a nanostructured matrix for Nb₂O₅ dispersive nanoparticles increase the overall pseudopacacitance in 63.2% for Nb₂O₅/MWCNT compared to MWCNT nanostructured electrodes. As observed in Fig. S2d, any faradaic reaction is undertaken at 3.0 V, and gravimetric current values are near 0 A $\rm g^{-1}$ soon after 25 s. Therefore, no gas could be observed, significantly decreasing the constant phase exponent values. As a result, MWCNT and Nb2O5/MWCNT nanostructured electrodes presented similar phase exponent values, deviating only 1.5%. Freitas et al. observed similar results for constant phase exponent behavior by studying water-splitting reaction onto TiO2nanotubes [74]. Also, it is possible to notice a decrease near 35% for charge transfer resistance related to Nb₂O₅/MWCNT compared to MWCNT nanostructured electrodes.

 $\label{eq:continuous} \begin{tabular}{ll} \textbf{Table 2} \\ \textbf{Statistical} \ and \ two-channel \ transmission \ line \ impedance \ parameters \ for \ Nb_2O_5/MWCNT \ nanostructured \ electrodes. \end{tabular}$

TL parameters/electrode material	MWCNT	MWCNT/Nb ₂ O ₅
χ^2	0.9996	0.9998
$r_{ m Electrolyte}/{ m m}\Omega$ g	7.14	8.80
$r_{ m Pore}/{ m m}\Omega$ g	16.50	20.58
$\overline{C}_{dl}/Fg^{-1}$	3.106	5.067
φ	0.972	0.956
$r_{ m ct}/\Omega$ g	49.75	17.0
$r_{Material}/\Omega$ g 10^{-8}	3.55	0.30

Moreover, lower charge transfer resistance led to lower materials resistance. Therefore, it is possible to observe one-order decreasing for the $Nb_2O_5/MWCNT$ compared to MWCNT nanostructured materials. These values were similar to those reported in the literature [75]. Finally, a remarkable difference on the Nyquist spectra towards the frequency range where the 45° at high frequency is located is observed.

It is possible to notice in Fig. 5 that the frequency range located on the Nyquist spectra related to 45° at high frequency is shifted to a lower frequency for Nb $_2$ O $_5$ /MWCNT compared to MWCNT nanostructured electrode. It is related to the finite-length transmission line model of diffusion-reaction impedance with absorbing boundary conditions presented by MWCNT nanostructured electrodes. Indeed, as observed at a high-frequency, MWCNT nanostructured electrodes showed anomalous

diffusion impedance [30,72,76,77]. Anomalous diffusion is represented by a mean squared displacement of the diffusing particles that does not follow the ordinary linear law $\langle r^2 \rangle \propto t$ but, in the most of cases, has a power-law dependence on time, and it is common in the diffusion-limited processes [30,78]. Otherwise, the Nb₂O₅/MWCNT nanostructured electrode presented a finite-length transmission line model of diffusion-reaction impedance with reflective boundary conditions. The diffusion-recombination impedance provides two basic kinds of spectra according to the conditions of Eq. (S26):

$$R_{rec} = \frac{\tau_f}{C_\mu^{cb}},\tag{21}$$

where, $r_{\rm rec}$ C_{μ} , and τ is the recombination resistance, chemical

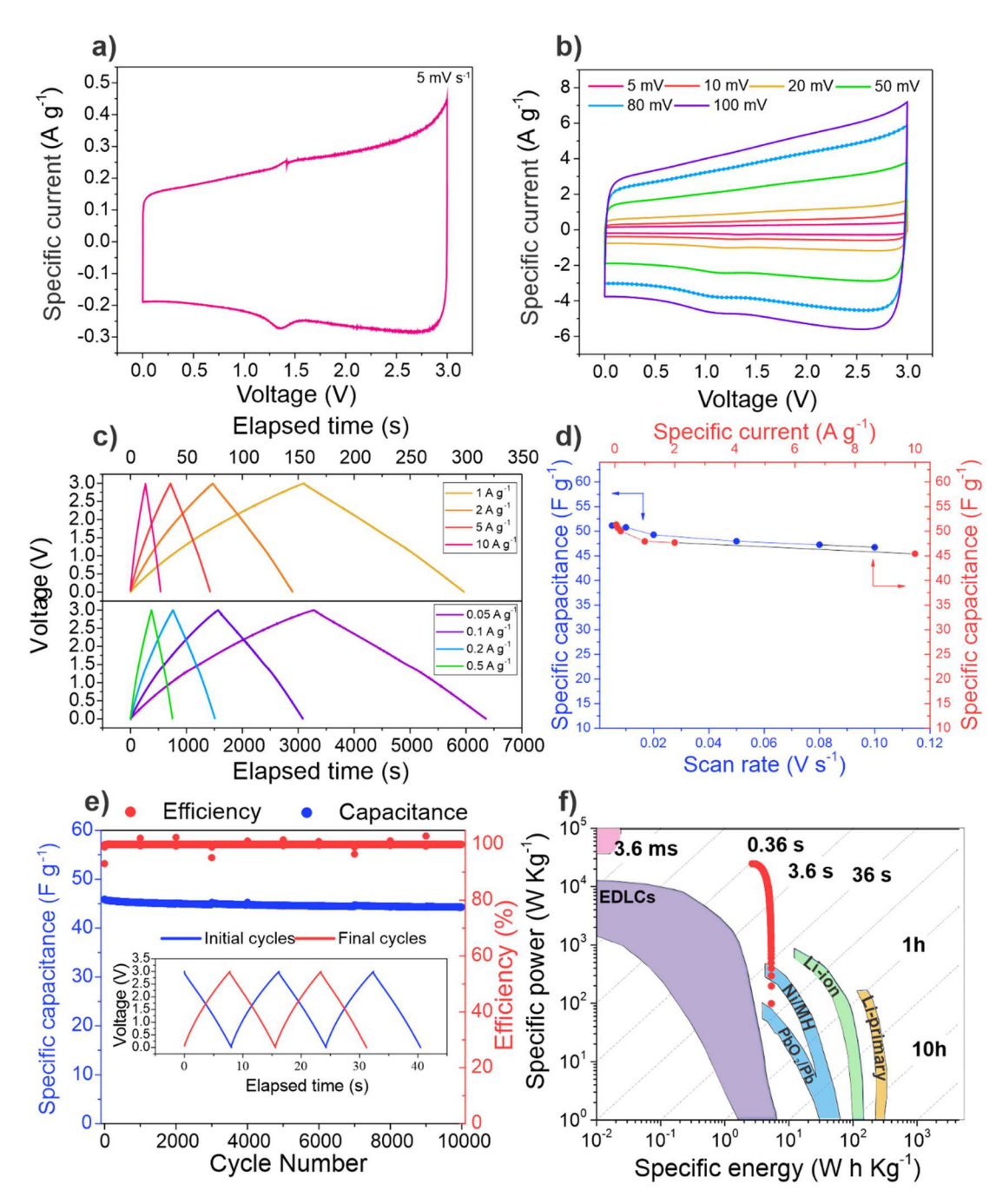


Fig. 6. Electrochemical performance in coin cell Nb₂O₅/MWCNT electrode filled with 1 M NaClO₄ EC:DMC (a & b) voltammetric profile at 5, 10, 20, 50, 80 and 100 mVs⁻¹, (c) galvanostatic charge-discharge curves with different currents (0.05, 0.1, 0.2, 0.5, 1, 2, 5 and 10 A g⁻¹), (d) Capacitance values as a function of scan rate and current density, (e) Cycling performance and (f) Ragone plot.

capacitance and lifetime, respectively.

For the case of a long diffusion length, the spectrum for which $r_{\rm tr} < r_{\rm rec}$, as displayed in Fig. 5, contains the characteristic Warburg impedance of diffusion, with an inclination of 45° at high frequency, which turns into an arc at low frequency. The arc is obtained from the pattern expression:

$$Z = \frac{1}{3} R_{tr} + \frac{R_{rec}}{1 + \frac{i\omega}{2c_{tr}}},\tag{22}$$

If the resistances $r_{\rm tr}$ and $r_{\rm rec}$ can be determined from the spectra, as shown in Fig. 5f then the diffusion length can be given by the expression derived from Equation:

$$L_n = \left(\frac{R_{rec}}{R_{tr}}\right)^{1/2} L,\tag{23}$$

However, if the conductivity is large, the transport resistance vanishes and cannot be noticed, as shown in Fig. 5e. Therefore, only diffusion length related to Nb₂O₅/MWCNT nanostructured electrodes $L_{\rm n}=13.5L$ was possible to be calculated. As a result, the Nyquist spectra observed for MWCNT nanostructured electrodes will indicate strong recombination and, consequently, according to Eq. (S25), $L_{\rm n}$, diffusion lengths are smaller than the active film thickness. On the contrary, the profile of Nyquist spectra presented by Nb₂O₅/MWCNT nanostructured electrodes indicates that the material is able Na⁺-ion diffusion.

Fig. 6 presents the electrochemical performance of Nb₂O₅/MWCNT electrodes in symmetrical coin cells. Here, the electrochemical results, including the Ragone plot, were obtained from the electrodes' active material. Fig. 6a, b shows the CV profile obtained with different sweep rates (5, 10, 20, 50, 80 and 100 mV s⁻¹), reinforcing the high surface area electrode with excellent electronic and ionic conductivities. Fig. 6c shows the GCD curves evidencing a high degree of reversibility, with symmetric curves and 100% coulombic efficiency under several current densities. The specific capacitances were calculated from Eqs. (4), (5) and (6), and capacitance retention values were extracted from both CV and GCD tests. As shown in Fig. 6d, the cell capacitance is 48 F g^{-1} at 50mVs⁻¹ and capacitance remains at 45.4 F g⁻¹ at a current density of 10 A g^{-1} . Thus, electrode capacitance is 4 times that ~ 192 F g^{-1} [1]. The cell was also subjected to consecutive charging-discharging cycles up to 10,000 cycles, and the capacitance retention and efficiency were presented in Fig. 5e. It is possible to notice capacitance retention of ~96% and a coulombic efficiency of 99%, implying excellent cycling stability.

The Ragone plot can be explained as a "planar representation" of the stored specific energy (W h kg⁻¹) as a function of the specific power (W kg⁻¹) for different devices. As demonstrated by Vicentini et al. [2], a more realistic system performance analysis can be obtained from Eq. (7).

Besides that, as Gogotsi et al. [79] discussed, considering just the weight of active material to report the Ragone plot does not give the device a realistic performance. So, for consistent energy and power densities, we also divided the values by a factor of 12 [79]. The present finding (Fig. 6f) shows that the assembled symmetric Nb₂O₅/MWCNT cell delivers a high energy density of 5.34 W h kg⁻¹ at a power density of 98.68 W kg⁻¹. Even with a power density of 24,671 W kg⁻¹, it delivers a high energy density of 2.67 W h kg⁻¹.

3.2.2. Na⁺-ion battery properties

The slurry coating or paint like coating is the most common method for preparation and electrochemical testing of electrochemically active materials. In our case, we first prepared one such electrode consisting of Nb_2O_5 particles to understand the electrochemical performance of the oxide material itself. Electrochemical data obtained using an electrode containing Nb_2O_5 coating are gathered in Fig. 7.

From the galvanostatic charge-discharge profiles, Fig. 7a, it is possible to observe the first 5 cycles of the cell with 25 mA g $^{-1}$ at 2.25 V. The Na $^{+}$ -ion insertion/extraction curves show a continuous change upon the cycles without exhibiting a distinct plateau region. This may indicate a capacitive contribution as a reaction mechanism between the Na $^{+}$ -ions and the electrode surface [80]. The Nb₂O₅ coating delivers a reversible capacity of 32 mA h g $^{-1}$ in the fifth cycle. It shows long-term cycle stability up to 100 cycles without significant capacity decay at a current density of 25 mA g $^{-1}$. As shown in Fig. 7b, at the end of cycling, the device has a capacity of 9.7 mA h g $^{-1}$ and an efficiency of \sim 92%.

Here, we hypothesize that a freestanding electrode of Nb_2O_5 supported with carbon nanotube network may improve electrode performance related to reversible capacity, cyclability and rate capability [81–83]. Therefore, electrochemical experiments were realized with two other half-cells using MWCNT and $Nb_2O_5/MWCNT$ nanostructured buckypaper as working electrodes. The electrochemical results are presented in Fig. 8. The mass used to obtain the gravimetric capacity and current was the electrode's total mass to provide a fairer comparison between the cells.

Fig. 8a, b present galvanostatic charge-discharge profiles with a 25 mA $\rm g^{-1}$ at 2.25 V from the two cells, respectively. In both cases, the first cycle presented an irreversible capacity. This behavior can be caused by the generation of a solid electrolyte interface (SEI) on the electrode surface due to the decomposition of the organic electrolyte and the irreversible Na⁺-ion insertion in the surface groups of the carbon material [21,56,84,85]. After the first cycle, Na⁺-ion insertion reactions become reversible. The Na⁺-ion insertion/extraction curves show a pseudo-linear voltage response without a distinctive plateau in both cases. The cell containing the Nb₂O₅/MWCNT electrode presents a

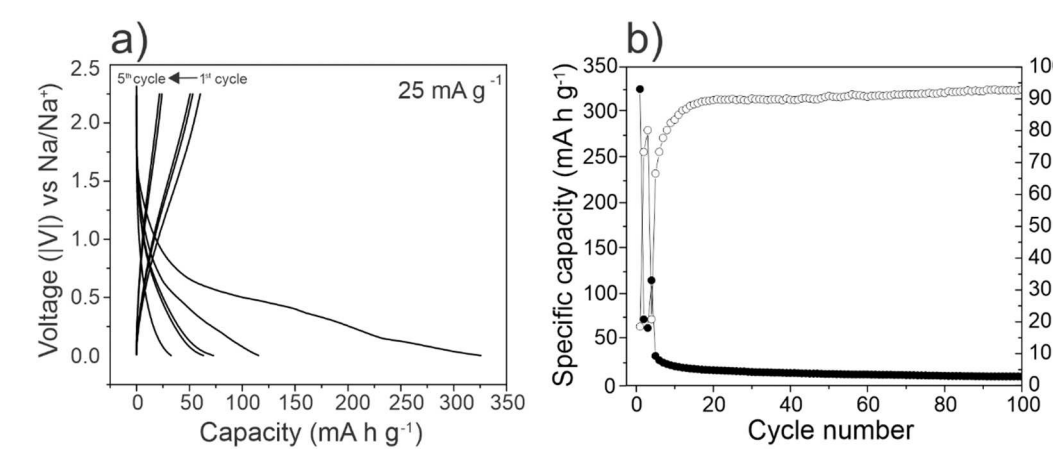


Fig. 7. Electrochemical performance in a sodium half-cell containing the Nb_2O_5 coated copper foil as an electrode and filled with 1 M $NaClO_4$ EC:DMC (a) Charge and discharge profile at a work voltage window of 2.25 V and specific current of 25 mA g^{-1} (b) Cycling performance up to 100 cycles and the initial and final cycles profile (c & d).

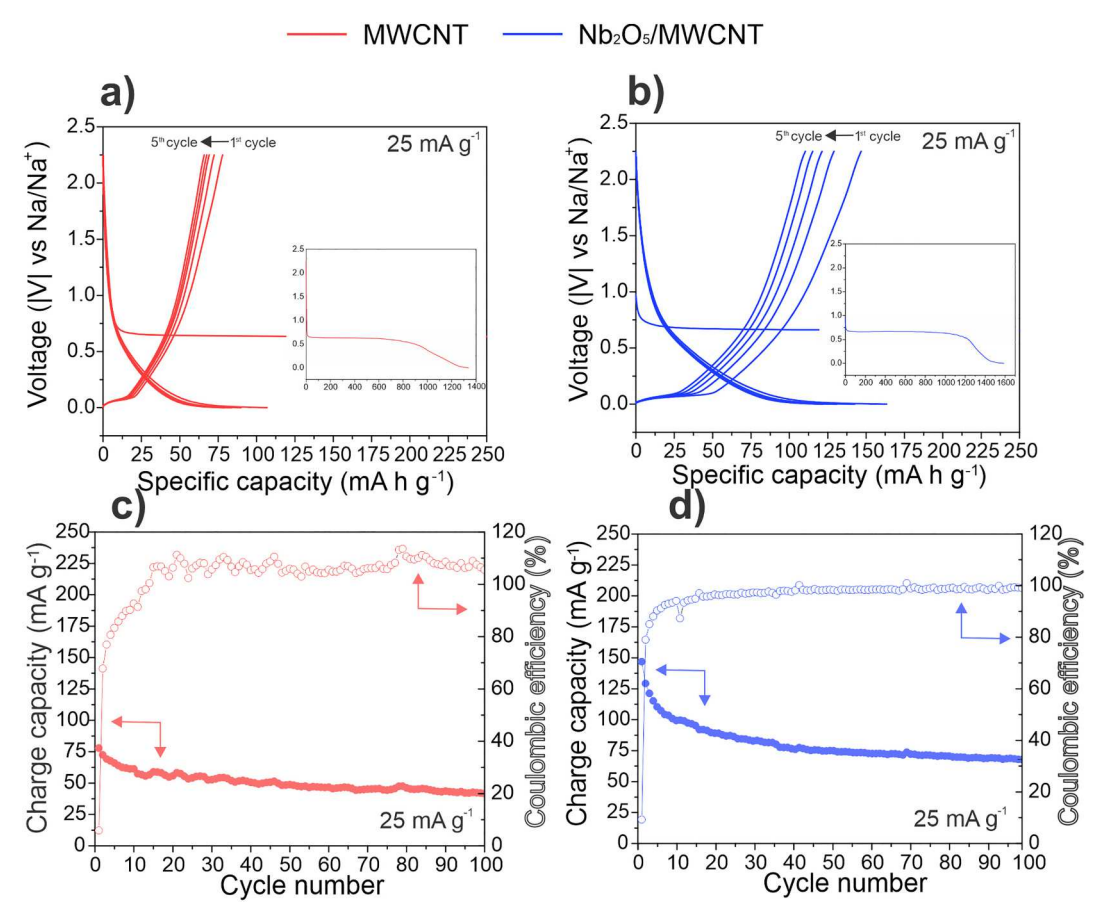


Fig. 8. Electrochemical tests comparing the MWCNT and $Nb_2O_5/MWCNT$ as an electrode in a sodium half-cell filled with 1 M NaClO₄ EC:DMC at the same conditions (a) charge-discharge profile from the first to the fifth cycle of MWCNT electrode (b) of $Nb_2O_5/MWCNT$ electrode (c-d) Cycling performance until 100 cycles of MWCNT and of $Nb_2O_5/MWCNT$ cells, respectively.

specific capacity of 163~mA h g $^{-1}$ in the second cycle. In comparison, the cell containing the MWCNT electrode has a capacity of 106~mA h g $^{-1}$. A significant improvement of 50% of the capacity from the cell of Nb $_2$ O $_5$ / MWCNT nanostructured electrodes is measured.

Fig. 8c, d shows the retention of the capacity of both cells, respectively. The Nb₂O₅/MWCNT electrode delivered a reversible capacity of 68 mA h g⁻¹ (100% of coulombic efficiency), contrasting with MWCNT electrode, which provided a 39 mA h g⁻¹. Besides that, it is possible to notice cycling stability and, consequently, linearity of the coulombic efficiency presented by the Nb₂O₅/MWCNT electrode differently from the MWCNT. This shows that Nb₂O₅ improves the stability of the Nb₂O₅/MWCNT cell, as also reported by [17,86–89]. Chen et al. attributed this to the special atomic arrangement of the T-Nb₂O₅ determinant to the ion migration and fast kinetics [86].

The differential capacity curves from the three SIBs cells (Nb₂O₅ slurry coated, MWCNT and Nb₂O₅/MWCNT) are shown in Fig. S4 of the Supporting information Section VII. From these, it is possible to notice irreversible reactions related to the formation of the solid electrolyte interface (SEI) during the first cycle due to the greater value of dQ/dV. The slight oxidation peak at 0.07 can be associated to the presence of functional groups in the carbon nanotube nanostructure since it is noticed as it is noticed both in the cell containing MWCNT and in the Nb₂O₅/MWCNT. Interestingly, the insertion of the Na⁺ into Nb₂O₅ did not show characteristics redox peaks, evidencing the crystalline Nb₂O₅ and its sodiated phase are miscible [20,90].

4. Conclusions

This research reported a freestanding and robust Nb₂O₅

nanoparticle-decorated MWCNT as electrode materials for a sodium-ion SIC and half-cell sodium-ion battery. Materials and devices were characterized, and results indicated intercalation of Na^+ into $\mathrm{Nb_2O_5}$ as a fast-charge faradaic process that considerably increases the capacitance/capacity of a carbon-based capacitor and battery.

Niobium pentoxide nanostructure properties were analyzed by XRD and Rietveld refinement, which allowed investigation of the structural and electronic properties of the $\mathrm{Nb_2O_5}$ that directly influence $\mathrm{Na^+}$ -ion diffusion. Results revealed that the material has two crystalline phases, orthorhombic and monoclinic, with a particle size of 70 nm and 52 nm, respectively. In addition, as presented in Table 1, the substantial weight fraction of the T-Nb₂O₅ crystalline phase (61.82%) resulted in improved ESD performance when d(001) T-Nb₂O₅ > d(001) H-Nb₂O₅.

The Nb₂O₅/MWCNT material was used as the electrodes in an SIC, and analysis in the frequency domain applied the EIS technique as a finite-length TL. The Nb₂O₅/MWCNT nanostructured electrode presented a finite-length TL model of diffusion-reaction impedance with reflective boundary conditions. Numerical modelling of the Nb₂O₅/MWCNT nanostructured electrodes showed Na⁺-ion diffusion. More specifically, the Nb₂O₅ increased the overall pseudocapacitance by 63.2% compared to MWCNT nanostructured electrodes. Overall, the SIC coin cell device (full cell) presented a maximum energy density of \sim 64 W h kg $^{-1}$ and a maximum power density of 15 kW kg $^{-1}$ in a long lifespan, as shown in the Ragone plot in Fig. 5f. This work paths the way to combine the best properties of supercapacitor and battery devices.

CRediT authorship contribution statement

Carla G. Real: Conceptualization, Methodology, Validation,

Investigation, Data curation, Writing – original draft, Writing – review & editing, Visualization, Project administration. Ericson H.N.S. Thaines: Formal analysis, Writing – review & editing. Leandro A. Pocrifka: Formal analysis, Writing – review & editing. Renato G. Freitas: Methodology, Formal analysis, Resources, Writing – review & editing, Supervision, Project administration, Funding acquisition. Gurpreet Singh: Conceptualization, Methodology, Investigation, Resources, Writing – original draft, Writing – review & editing, Supervision, Project administration, Funding acquisition. Hudson Zanin: Conceptualization, Methodology, Investigation, Resources, Writing – original draft, Writing – review & editing, Supervision, Project administration, Funding acquisition.

Declaration of competing interest

The authors declare that they have no known competing financial interests or personal relationships that could have appeared to influence the work reported in this paper.

Acknowledgements

The authors are very grateful for the financial support from the Brazilian funding agencies CNPq (310544/2019-0 - PQ-2 grant), CAPES PROEX 88887.374731/2019-00, Print-CAPES (8887.572651/2020-00) and FAPESP (2017/11958-1 & 2014/02163-7). The authors gratefully acknowledge the support Shell and the strategic importance of the support given by ANP (Brazil's National Oil, Natural Gas and Biofuels Agency) through the R&D levy regulation. R. G. Freitas wishes to thank CNPq (PQ-2 grant: Process 304442/2019-4). This study was financed in part by the CAPES (Brazil) - Finance Code 001.

Appendix A. Supplementary data

Supplementary data to this article can be found online at https://doi.org/10.1016/j.est.2022.104793.

References

- F. Béguin, E. Frackowiak, Supercapacitors: Materials, Systems, and Applications, Wiley-VCH Verlag GmbH & Co. KGaA, Weinheim, Germany, 2013, https://doi. org/10.1002/9783527646661.
- [2] R. Vicentini, J.P. Aguiar, R. Beraldo, R. Venâncio, F. Rufino, L.M. Da Silva, H. Zanin, Ragone plots for electrochemical double-layer capacitors, Batter. Supercaps 4 (2021) 1291–1303, https://doi.org/10.1002/BATT.202100093.
- [3] B.E. Conway, Electrochemical Supercapacitors, SpringerUS, 1999, https://doi.org/ 10.1007/978-1-4757-3058-6.
- [4] L.M. Da Silva, R. Cesar, C.M.R. Moreira, J.H.M. Santos, L.G. De Souza, B.M. Pires, R. Vicentini, W. Nunes, H. Zanin, Reviewing the fundamentals of supercapacitors and the difficulties involving the analysis of the electrochemical findings obtained for porous electrode materials, Energy Storage Mater. 27 (2020) 555–590, https:// doi.org/10.1016/j.ensm.2019.12.015.
- [5] W.G. Nunes, A.N. Miranda, B. Freitas, R. Vicentini, A.C. Oliveira, G. Doubek, R. G. Freitas, L.M. Da Silva, H. Zanin, Charge-storage mechanism of highly defective NiO nanostructures on carbon nanofibers in electrochemical supercapacitors, Nanoscale 13 (2021) 9590–9605, https://doi.org/10.1039/d1nr00065a.
- [6] T. Liu, L. Finn, M. Yu, H. Wang, T. Zhai, X. Lu, Y. Tong, Y. Li, Polyaniline and polypyrrole pseudocapacitor electrodes with excellent cycling stability, Nano Lett. 14 (2014) 2522–2527, https://doi.org/10.1021/nl500255v.
- [7] C. Costentin, J.M. Savéant, Energy storage: pseudocapacitance in prospect, Chem. Sci. 10 (2019) 5656–5666, https://doi.org/10.1039/c9sc01662g.
- [8] X. Han, Q. Meng, X. Wan, B. Sun, Y. Zhang, B. Shen, J. Gao, Y. Ma, P. Zuo, S. Lou, G. Yin, Intercalated pseudocapacitive electrochemistry of nb-based oxides for fast charging of lithium-ion batteries, Nano Energy 81 (2021), 105635, https://doi. org/10.1016/j.nanoen.2020.105635.
- [9] A. Noori, M.F. El-Kady, M.S. Rahmanifar, R.B. Kaner, M.F. Mousavi, Towards establishing standard performance metrics for batteries, supercapacitors and beyond, Chem. Soc. Rev. 48 (2019) 1272–1341, https://doi.org/10.1039/ c8cs00581h.
- [10] T.F. Yi, H.M.K. Sari, X. Li, F. Wang, Y.R. Zhu, J. Hu, J. Zhang, X. Li, A review of niobium oxides based nanocomposites for lithium-ion batteries, sodium-ion batteries and supercapacitors, Nano Energy 85 (2021), 105955, https://doi.org/ 10.1016/j.nanoen.2021.105955.

- [11] B.L. Ellis, L.F. Nazar, Sodium and sodium-ion energy storage batteries, Curr. Opin. Solid State Mater. Sci. 16 (2012) 168–177, https://doi.org/10.1016/j. cosps. 2012 04.002
- [12] C. Vaalma, D. Buchholz, M. Weil, S. Passerini, A cost and resource analysis of sodium-ion batteries, Nat. Rev. Mater. 3 (2018) 1–11, https://doi.org/10.1038/ natrevmats.2018.13.
- [13] P.K. Nayak, L. Yang, W. Brehm, P. Adelhelm, From lithium-ion to sodium-ion batteries: advantages, challenges, and surprises, Angew. Chem. Int. Ed. 57 (2018) 102–120, https://doi.org/10.1002/anie.201703772.
- [14] C. Delmas, Sodium and sodium-ion batteries: 50 years of research, Adv. Energy Mater. 8 (2018), https://doi.org/10.1002/aenm.201703137.
- [15] R. Vicentini, W. Nunes, B.G.A. Freitas, L.M. Da Silva, D.M. Soares, R. Cesar, C. B. Rodella, H. Zanin, Niobium pentoxide nanoparticles @ multi-walled carbon nanotubes and activated carbon composite material as electrodes for electrochemical capacitors, Energy Storage Mater. 22 (2019) 311–322, https://doi.org/10.1016/j.ensm.2019.08.007.
- [16] R. Vicentini, D.M. Soares, W. Nunes, B. Freitas, L. Costa, L.M. Da Silva, H. Zanin, Core-niobium pentoxide carbon-shell nanoparticles decorating multiwalled carbon nanotubes as electrode for electrochemical capacitors, J. Power Sources 434 (2019), 226737, https://doi.org/10.1016/j.jpowsour.2019.226737.
- [17] V. Augustyn, J. Come, M.A. Lowe, J.W. Kim, P.L. Taberna, S.H. Tolbert, H. D. Abruña, P. Simon, B. Dunn, High-rate electrochemical energy storage through Li + intercalation pseudocapacitance, Nat. Mater. 12 (2013) 518–522, https://doi.org/10.1038/nmat3601.
- [18] G. Brauer, Die Oxyde des Niobs, Z. Anorg. Allg. Chem. 248 (1941) 1, https://doi. org/10.1002/ZAAC.19412480101.
- [19] L.K. Frevel, H.W. Rinn, Powder diffraction standards for niobium pentoxide and tantalum pentoxide, Anal. Chem. 27 (2002) 1329–1330, https://doi.org/10.1021/ AC60104A035.
- [20] J. Ni, W. Wang, C. Wu, H. Liang, J. Maier, Y. Yu, L. Li, Highly reversible and durable Na storage in niobium pentoxide through optimizing structure, composition, and nanoarchitecture, Adv. Mater. 29 (2017) 1605607, https://doi. org/10.1002/ADMA.201605607.
- [21] Z. Tong, S. Liu, Y. Zhou, J. Zhao, Y. Wu, Y. Wang, Y. Li, Rapid redox kinetics in uniform sandwich-structured mesoporous Nb2O5/graphene/mesoporous Nb2O5 nanosheets for high-performance sodium-ion supercapacitors, Energy Storage Mater. 13 (2018) 223–232, https://doi.org/10.1016/j.ensm.2017.12.005.
- [22] L. Yang, Y.-E. Zhu, J. Sheng, F. Li, B. Tang, Y. Zhang, Z. Zhou, T-Nb2O5/C nanofibers prepared through electrospinning with prolonged cycle durability for high-rate sodium-ion batteries induced by pseudocapacitance, Small 13 (2017) 1702588, https://doi.org/10.1002/SMLL.201702588.
- [23] L. Wang, X. Bi, S. Yang, Partially single-crystalline mesoporous Nb2O5 nanosheets in between graphene for ultrafast sodium storage, Adv. Mater. 28 (2016) 7672–7679, https://doi.org/10.1002/ADMA.201601723.
- [24] H.M. Rietveld, Line profiles of neutron powder-diffraction peaks for structure refinement, Acta Crystallogr. 22 (1967) 151–152, https://doi.org/10.1107/ S0365110X67000234.
- [25] C.G. Real, R. Vicentini, W.G. Nunes, A.M. Pascon, F.A. Campos, L.M. Da Silva, R. G. Freitas, H. Zanin, Analyses of dispersive effects and the distributed capacitance in the time and frequency domains of activated carbon nanofiber electrodes as symmetric supercapacitors, Electrochim. Acta (2021), 139299, https://doi.org/10.1016/J.FJECTACTA.2021.139299.
- [26] R. Vicentini, R. Beraldo, J.P. Aguiar, F.E. Oliveira, F.C. Rufino, D.R.G. Larrude, L. M. Da Silva, H. Zanin, Niobium pentoxide nanoparticles decorated graphene as electrode material in aqueous-based supercapacitors: accurate determination of the working voltage window and the analysis of the distributed capacitance in the time domain, J. Energy Storage 44 (2021), 103371, https://doi.org/10.1016/J. FST 2021 103371
- [27] R. de Levie, On porous electrodes in electrolyte solutions. I. Capacitance effects, Electrochim. Acta 8 (1963) 751–780, https://doi.org/10.1016/0013-4686(63) 80042-0.
- [28] U. Rammelt, G. Reinhard, The influence of surface roughness on the impedance data for iron electrodes in acid solutions, Corros. Sci. 27 (1987) 373–382, https:// doi.org/10.1016/0010-938X(87)90079-5.
- [29] J. Bisquert, G. Garcia-Belmonte, P. Bueno, E. Longo, L.O.S. Bulhões, Impedance of constant phase element (CPE)-blocked diffusion in film electrodes, J. Electroanal. Chem. 452 (1998) 229–234, https://doi.org/10.1016/S0022-0728(98)00115-6.
- [30] J. Bisquert, G. Garcia-Belmonte, F. Fabregat-Santiago, A. Compte, Anomalous transport effects in the impedance of porous film electrodes, Electrochem. Commun. 1 (1999) 429–435, https://doi.org/10.1016/S1388-2481(99)00084-3.
- [31] J. Bisquert, Influence of the boundaries in the impedance of porous film electrodes, Phys. Chem. Chem. Phys. 2 (2000) 4185–4192, https://doi.org/10.1039/ b001708f.
- [32] M.A. Santanna, W.T. Menezes, Y.V.B. Santana, M.M. Ferrer, A.F. Gouveia, A. D. Faceto, A.J. Terezo, A.J.A. Oliveira, E. Longo, R.G. Freitas, E.C. Pereira, The effect of TiO2 nanotube morphological engineering and ZnS quantum dots on the water splitting reaction: a theoretical and experimental study, Int. J. Hydrog. Energy 43 (2018) 6838–6850, https://doi.org/10.1016/j.ijhydene.2018.02.113.
- [33] L.F.Q.P. Marchesi, F.R. Simões, L.A. Pocrifka, E.C. Pereira, Investigation of polypyrrole degradation using electrochemical impedance spectroscopy, J. Phys. Chem. B 115 (2011) 9570–9575, https://doi.org/10.1021/JP2041263.
- [34] W.G. Nunes, L.M. Da Silva, R. Vicentini, B.G.A. Freitas, L.H. Costa, A.M. Pascon, H. Zanin, Nickel oxide nanoparticles supported onto oriented multi-walled carbon nanotube as electrodes for electrochemical capacitors, Electrochim. Acta 298 (2019) 468–483, https://doi.org/10.1016/j.electacta.2018.12.102.

- [35] W.G. Nunes, R. Vicentini, B.G.A. Freitas, F.E.R. Oliveira, A.M.P. Marque, R. M. Filho, G. Doubek, L.M. Da Silva, H. Zanin, Pseudo-capacitive behavior of multi-walled carbon nanotubes decorated with nickel and manganese (hydr)oxides nanoparticles, J. Energy Storage 31 (2020), 101583, https://doi.org/10.1016/j.est.2020.101583
- [36] R. Vicentini, W.G. Nunes, L.H. Costa, L.M. Da Silva, A. Pascon, P. Jackson, G. Doubek, H. Zanin, Highly stable nickel-aluminum alloy current collectors and highly defective multi-walled carbon nanotubes active material for neutral aqueous-based electrochemical capacitors, J. Energy Storage 23 (2019) 116–127, https://doi.org/10.1016/j.est.2019.01.013.
- [37] B. Freitas, W.G. Nunes, D.M. Soares, F.C. Rufino, C.M. Moreira, L.M. Da Silva, H. Zanin, Robust, flexible, freestanding and high surface area activated carbon and multi-walled carbon nanotubes composite material with outstanding electrode properties for aqueous-based supercapacitors, Mater. Adv. (2021), https://doi.org/ 10.1039/d0ma00783h
- [38] A.C. Larson, R.B. Von, D. Lansce, GSAS GENERAL STRUCTURE ANALYSIS SYSTEM, (n.d.).
- [39] B.H. Toby, EXPGUI, a graphical user interface for GSAS, J. Appl. Crystallogr. 34 (2001) 210–213, https://doi.org/10.1107/S0021889801002242.
- [40] P. Thompson, D.E. Cox, J.B. Hastings, Rietveld refinement of Debye-Scherrer synchrotron X-ray data from Al2O3, J. Appl. Crystallogr. 20 (1987) 79–83, https://doi.org/10.1107/S0021889887087090.
- [41] P.W. Stephens, in: Phenomenological Model of Anisotropic Peak Broadening in Powder Diffraction 32, 1999, pp. 281–289, https://doi.org/10.1107/ S0021889898006001. Urn:Issn:0021-8898.
- [42] G. Caglioti, A. Paoletti, F.P. Ricci, Choice of collimators for a crystal spectrometer for neutron diffraction, Nucl. Instrum. 3 (1958) 223–228, https://doi.org/ 10.1016/0369-643X(58)90029-X.
- [43] J. Bisquert, Theory of the impedance of electron diffusion and recombination in a thin layer, J. Phys. Chem. B 106 (2002) 325–333, https://doi.org/10.1021/ ip011941e.
- [44] R. Vicentini, J.Pedro Aguiar, R. Beraldo, R. Venâncio, F. Rufino, L.M.Da Silva, H. Zanin, "Ragone plots for electrochemical double-layer capacitors," Batter. Supercaps, May 2021.agone plots for electrochemical double-layer capacitors, Batter. Supercaps (2021), https://doi.org/10.1002/batt.202100093.
- [45] C. Glaize, S. Genies, in: Lithium Batteries and Other Electrochemical Storage Systems, 2013, p. 354.
- [46] R. Vicentini, L.M. Da Silva, D.V. Franco, W. Nunes, J. Fiates, G. Doubek, L.F. M. Franco, R.G. Freitas, C. Fantini, H. Zanin, Raman probing carbon & aqueous electrolytes interfaces and molecular dynamics simulations towards understanding electrochemical properties under polarization conditions in supercapacitors, J. Energy Chem. 60 (2021) 279–292, https://doi.org/10.1016/j.iechem.2021.01.003.
- [47] A.C. Ferrari, D.M. Basko, Raman spectroscopy as a versatile tool for studying the properties of graphene, Nat. Nanotechnol. 8 (2013) 235–246, https://doi.org/ 10.1038/nnano.2013.46.
- [48] L.G. Cançado, A. Jorio, E.H.M. Ferreira, F. Stavale, C.A. Achete, R.B. Capaz, M.V. O. Moutinho, A. Lombardo, T.S. Kulmala, A.C. Ferrari, Quantifying defects in graphene via Raman spectroscopy at different excitation energies, Nano Lett. 11 (2011) 3190–3196, https://doi.org/10.1021/nl201432g.
- [49] A.C. Ferrari, Raman spectroscopy of graphene and graphite: disorder, electron-phonon coupling, doping and nonadiabatic effects, Solid State Commun. 143 (2007) 47–57, https://doi.org/10.1016/j.ssc.2007.03.052.
 [50] T.A. Silva, H. Zanin, E. Saito, R.A. Medeiros, F.C. Vicentini, E.J. Corat, O. Fatibello-
- [50] T.A. Silva, H. Zanin, E. Saito, R.A. Medeiros, F.C. Vicentini, E.J. Corat, O. Fatibello-Filho, Electrochemical behaviour of vertically aligned carbon nanotubes and graphene oxide nanocomposite as electrode material, Electrochim. Acta 119 (2014) 114–119, https://doi.org/10.1016/j.electacta.2013.12.024.
 [51] A.O. Lobo, S.C. Ramos, E.F. Antunes, F.R. Marciano, V.J. Trava-Airoldi, E.J. Corat,
- [51] A.O. Lobo, S.C. Ramos, E.F. Antunes, F.R. Marciano, V.J. Trava-Airoldi, E.J. Corat Fast functionalization of vertically aligned multiwalled carbon nanotubes using oxygen plasma, Mater. Lett. 70 (2012) 89–93, https://doi.org/10.1016/j. matlet.2011.11.071.
- [52] H. Zanin, C.M.R. Rosa, N. Eliaz, P.W. May, F.R. Marciano, A.O. Lobo, Assisted deposition of nano-hydroxyapatite onto exfoliated carbon nanotube oxide scaffolds, Nanoscale 7 (2015) 10218–10232, https://doi.org/10.1039/ c4m07317e
- [53] M.A.V.M. Grinet, H. Zanin, A.E. Campos Granato, M. Porcionatto, F.R. Marciano, A.O. Lobo, Fast preparation of free-standing nanohydroxyapatite-vertically aligned carbon nanotube scaffolds, J. Mater. Chem. B 2 (2014) 1196–1204, https://doi. org/10.1039/c3tb21525c.
- [54] A.A. McConnell, J.S. Aderson, C.N.R. Rao, Raman spectra of niobium oxides, Spectrochim. Acta Part A Mol.Spectrosc. 32 (1976) 1067–1076, https://doi.org/ 10.1016/0584-8539(76)80291-7.
- [55] R. Brayner, F. Bozon-Verduraz, Niobium pentoxide prepared by soft chemical routes: morphology, structure, defects and quantum size effect, Phys. Chem. Chem. Phys. 5 (2003) 1457–1466, https://doi.org/10.1039/b210055j.
- [56] Y. Wu, X. Fan, R.R. Gaddam, Q. Zhao, D. Yang, X. Sun, C. Wang, X.S. Zhao, Mesoporous niobium pentoxide/carbon composite electrodes for sodium-ion capacitors, J. Power Sources 408 (2018) 82–90, https://doi.org/10.1016/j. jpowsour.2018.10.080.
- [57] H. Yang, H. Xu, L. Wang, L. Zhang, Y. Huang, X. Hu, Microwave-assisted rapid synthesis of self-assembled T-Nb2O5 nanowires for high-energy hybrid supercapacitors, Chem. Eur. J. 23 (2017) 4203–4209, https://doi.org/10.1002/ chem. 2017/0010
- [58] G.H.de M. Gomes, N.D.S. Mohallem, Investigation of phase transition employing strain mapping in TT- and T-Nb2O5 obtained by HRTEM micrographs, Micron 148 (2021), 103112, https://doi.org/10.1016/J.MICRON.2021.103112.

- [59] R.A. Ismail, E.T. Salim, H.T. Halbos, Preparation of Nb2O5 nanoflakes by hydrothermal route for photodetection applications: the role of deposition time, Optik (Stuttg). 245 (2021), 167778, https://doi.org/10.1016/J. JULEO 2021 167778
- [60] Y. Wen, K. He, Y. Zhu, F. Han, Y. Xu, I. Matsuda, Y. Ishii, J. Cumings, C. Wang, Expanded graphite as superior anode for sodium-ion batteries, Nat. Commun. 5 (2014) 1–10, https://doi.org/10.1038/ncomms5033, 2014 51.
- [61] Y. Cao, L. Xiao, M.L. Sushko, W. Wang, B. Schwenzer, J. Xiao, Z. Nie, L.V. Saraf, Z. Yang, J. Liu, Sodium ion insertion in hollow carbon nanowires for battery applications, Nano Lett. 12 (2012) 3783–3787, https://doi.org/10.1021/NI.3016957.
- [62] D. Billaud, L. Thevenot, P. Willmann, Synthesis and characterization of a new lithium-rich graphite intercalation compound: Li2C6Oy (y≈0.5), New J. Chem. 22 (1998) 1417–1420, https://doi.org/10.1039/A804644A.
- [63] M.B. Pinto, J.Antonio Lenito Soares, A.M. Orellana, H.A. Duarte, H.A.De Abreu, Structural, electronic, and thermodynamic properties of the T and B phases of Niobia: first-principle calculations, J. Phys. Chem. A 121 (2017) 2399–2409, https://doi.org/10.1021/ACS_JPCA.6B11383.
- [64] Z. Yao X. Xia S. Zhang C. Zhou G. Pan ... Q.X.-E.S., undefined 2020, Oxygen defect boosted N-doped Ti2Nb10O29 anchored on core-branch carbon skeleton for both high-rate liquid & solid-state lithium ion batteries, Elsevier. (n.d.). https://www.sciencedirect.com/science/article/pii/S240582971930981X?casa_token=NTvcnGsC-CwAAAAA: kqfOy6roQX0Glal6VmmL1LWXzG7jBTgaKbgmDfACLc-66lgrggFliIEDc3op0Ussx3bodOv16w (accessed December 24, 2021).
- [65] Y. Lian, N. Yang, D. Wang, Y. Zheng, C. Ban, J. Zhao, H. Zhang, Optimization design and application of niobium-based materials in electrochemical energy storage, Adv. Energy Sustain. Res. 1 (2020), 2000038, https://doi.org/10.1002/ ARSP. 20200033
- [66] Fei Shen, Zhongti Sun, Qinggang He, Jingyu Sun, R.B. Kaner, Yuanlong Shao, Niobium pentoxide based materials for high rate rechargeable electrochemical energy storage, Mater. Horiz. 8 (2021) 1130–1152, https://doi.org/10.1039/ D0MH01481H.
- [67] S. Li, T. Wang, W. Zhu, J. Lian, Y. Huang, Y.-Y. Yu, J. Qiu, Y. Zhao, Y.-C. Yong, H. Li, Controllable synthesis of uniform mesoporous H-Nb2O5/rGO nanocomposites for advanced lithium ion hybrid supercapacitors, J. Mater. Chem. A 7 (2019) 693–703, https://doi.org/10.1039/C8TA10239B.
- [68] X. Liu, G. Liu, Y. Liu, R. Sun, J. Ma, J. Guo, M. Hu, Urchin-like hierarchical H-Nb2O5 microspheres: synthesis, formation mechanism and their applications in lithium ion batteries, Dalt. Trans. 46 (2017) 10935–10940, https://doi.org/10.1039/C7DT02021J.
- [69] N. Li, F. Zhang, Y. Tang, Hierarchical T-Nb2O5 nanostructure with hybrid mechanisms of intercalation and pseudocapacitance for potassium storage and high-performance potassium dual-ion batteries, J. Mater. Chem. A 6 (2018) 17889–17895. https://doi.org/10.1039/C8TA07987K.
- [70] J.W. Kim, V. Augustyn, B. Dunn, The effect of crystallinity on the rapid pseudocapacitive response of Nb2O5, Adv. Energy Mater. 2 (2012) 141–148, https://doi.org/10.1002/AENM.201100494.
- [71] R.B. Kaner, Yuanlong Shao, Fabrication of Nb2O5 nanosheets for high-rate lithium ion storage applications, Sci. Rep. 5 (2015) 1–6, https://doi.org/10.1038/ srep08326. 2015 51.
- [72] G. Garcia-Belmonte, J. Bisquert, E.C. Pereira, F. Fabregat-Santiago, Anomalous transport on polymeric porous film electrodes in the dopant-induced insulator-toconductor transition analyzed by electrochemical impedance, Appl. Phys. Lett. 78 (2001) 1885–1887, https://doi.org/10.1063/1.1354671.
- [73] J. Bisquert, G. Garcia-Belmonte, F. Fabregat-Santiago, N.S. Ferriols, P. Bogdanoff, E.C. Pereira, Doubling exponent models for the analysis of porous film electrodes by impedance. Relaxation of TiO2 nanoporous in aqueous solution, J. Phys. Chem. B 104 (2000) 2287–2298, https://doi.org/10.1021/jp993148h.
- [74] R.G. Freitas, M.A. Santanna, E.C. Pereira, Dependence of TiO2 nanotube microstructural and electronic properties on water splitting, J. Power Sources 251 (2014) 178–186, https://doi.org/10.1016/j.jpowsour.2013.11.067.
- [75] S. Zhang, N. Nguyen, B. Leonhardt, C. Jolowsky, A. Hao, J.G. Park, R. Liang, Carbon-nanotube-based electrical conductors: fabrication, optimization, and applications, Adv. Electron. Mater. 5 (2019), 1800811, https://doi.org/10.1002/ AELM.201800811.
- [76] G. Paasch, K. Micka, P. Gersdorf, Theory of the electrochemical impedance of macrohomogeneous porous electrodes, Electrochim. Acta 38 (1993) 2653–2662, https://doi.org/10.1016/0013-4686(93)85083-B.
- [77] * Rama Kant, Rajesh Kumar, V.K. Yadav, Theory of anomalous diffusion impedance of realistic fractal electrode, J. Phys. Chem. C 112 (2008) 4019–4023, https://doi. org/10.1021/JP712066K.
- [78] T. Pajkossy, L. Nyikos, Impedance of planar electrodes with scale-invariant capacitance distribution, J. Electroanal. Chem. 332 (1992) 55–61, https://doi.org/ 10.1016/0022-0728(92)80340-A.
- [79] Y. Gogotsi, P. Simon, True performance metrics in electrochemical energy storage, Science 334 (2011) 917–918, https://doi.org/10.1126/science.1213003.
- [80] J. Come, V. Augustyn, J. Woung Kim, P. Rozier, P.-L. Taberna, P. Gogotsi, J. W. Long, B. Dunn, Electrochemical kinetics of nanostructured Nb2O5 electrodes, J. Electrochem. Soc. 161 (2014), https://doi.org/10.1149/2.040405jesï.
- [81] S. Mukherjee S. Bin Mujib D. Soares G.S.- Materials, undefined 2019, Electrode Materials for High-Performance Sodium-Ion Batteries, Mdpi.Com. (n.d.). https:// www.mdpi.com/1996-1944/12/12/1952 (accessed September 1, 2020).
- [82] L. David, D. Asok, G. Singh, Synthesis and extreme rate capability of Si-Al-C-N functionalized carbon nanotube spray-on coatings as li-ion battery electrode, ACS

- Appl. Mater. Interfaces 6 (2014) 16056–16064, https://doi.org/10.1021/
- [83] Y. Li, Y. Lu, C. Zhao, Y.S. Hu, M.M. Titirici, H. Li, X. Huang, L. Chen, Recent advances of electrode materials for low-cost sodium-ion batteries towards practical application for grid energy storage, Energy Storage Mater. 7 (2017) 130–151, https://doi.org/10.1016/j.ensm.2017.01.002.
- [84] Y. Li, H. Wang, L. Wang, Z. Mao, R. Wang, B. He, Y. Gong, X. Hu, Mesopore-induced ultrafast Na+-storage in T-Nb205/carbon nanofiber films toward flexible high-power Na-ion capacitors, Small 15 (2019), 1804539, https://doi.org/10.1002/smll.201804539.
- [85] E. Lim, J. Changshin, M.S. Kim, M.H. Kim, J. Chun, H. Kim, J. Park, K.C. Roh, K. Kang, S. Yoon, J. Lee, High-performance sodium-ion hybrid supercapacitor based on Nb2O5@carbon core-shell nanoparticles and reduced graphene oxide nanocomposites, Adv. Funct. Mater. 26 (2016) 3711–3719, https://doi.org/10.1002/adfm.201505548.
- [86] D. Chen, J.H. Wang, T.F. Chou, B. Zhao, M.A. El-Sayed, M. Liu, Unraveling the nature of anomalously fast energy storage in T-Nb2O5, J. Am. Chem. Soc. 139 (2017) 7071–7081, https://doi.org/10.1021/JACS.7B03141/SUPPL_FILE/ JA7B03141_SI_003.TXT.

- [87] W. Zhang, L. Xiao, J. Zheng, Y. Zhong, B. Shi, H. Chen, H. Fu, Effect of Nb2O5 nanocoating on the thermal stability and electrochemical performance of LiNi0.6Co0.2Mn0.2O2 cathode materials for lithium ion batteries, J. Alloys Compd. 880 (2021), 160415, https://doi.org/10.1016/J.JALLCOM.2021.160415.
- [88] Q. Deng, F. Chen, S. Liu, A. Bayaguud, Y. Feng, Z. Zhang, Y. Fu, Y. Yu, C. Zhu, Advantageous functional integration of adsorption-intercalation-conversion hybrid mechanism in 3D flexible Nb2O5@hard carbon@MoS2@Soft carbon fiber paper anodes for ultrafast and super-stable sodium storage, Adv. Funct. Mater. 30 (2020), 1908665, https://doi.org/10.1002/ADFM.201908665.
- [89] X. Wang, G. Li, Z. Chen, V. Augustyn, X. Ma, G. Wang, B. Dunn, Y. Lu, High-performance supercapacitors based on nanocomposites of Nb2O5 nanocrystals and carbon nanotubes, Adv. Energy Mater. 1 (2011) 1089–1093, https://doi.org/10.1002/AENM.201100332.
- [90] G. Rousse, M.E. Arroyo-De Dompablo, P. Senguttuvan, A. Ponrouch, J.M. Tarascon, M.R. Palacín, Rationalization of intercalation potential and redox mechanism for A 2Ti3O7 (A = Li, Na), Chem. Mater. 25 (2013) 4946–4956, https://doi.org/ 10.1021/CM4032336.